An Optical CMM for Flexible On-Machine Inspection

by

Eric Buckley

B.A.Sc., The University of British Columbia, 2012

A THESIS SUBMITTED IN PARTIAL FULFILLMENT OF

THE REQUIREMENTS FOR THE DEGREE OF

MASTER OF APPLIED SCIENCE

in

THE FACULTY OF GRADUATE AND POSTDOCTORAL STUDIES

(Mechanical Engineering)

THE UNIVERSITY OF BRITISH COLUMBIA

(Vancouver)

April 2018

Abstract

This thesis presents the design and testing results of an optical coordinate measurement machine for on-machine inspection of machined parts. Inspecting parts on the machine which produces them avoids lost productivity by identifying malfunctioning production machines quickly, thereby reducing the number of out of spec parts produced. The optical coordinate measurement machine designed for this project uses two cameras to track a handheld probe which is used to probe the inspected part. The cameras are designed specifically for the project. They are able to capture target measurements at a very high frequency, which allows averaging of many measurements for increased accuracy. Inspecting parts on-machine requires the system configuration to be flexible, as different machines will need to have the cameras in different locations relative to one another. The cameras are designed to communicate using the flexible EtherCAT fieldbus protocol, and are attached to a modular frame, so that the system can be reconfigured. The probe has four LED targets which are tracked by the cameras and a stylus tip with a probing ball.

The reconstruction of the probe tip position requires two stages. First the LED target positions are calculated from the camera measurements using a camera model, and then a geometric fitting is done to match the known probe geometry to the measurements and find the probe tip location. The reconstruction is done by software running in the TwinCAT real-time operating system on a host PC. The calibration of the camera model parameters is done using a CMM with <5 µm accuracy. The accuracy of the camera calibration is 23.6 µm at a distance of 1m from the cameras. The probe is calibrated using a procedure developed by the author. The probe ball center calibration accuracy is estimated to be less than 10 µm.

The system is tested by performing a series of measurement tasks probing flat and spherical surfaces. The system shows an accuracy of 30 μm for these tasks.

Lay Summary

This thesis presents the design and testing results of a machine which uses a pair of cameras and a handheld probe to measure the dimensions of parts. Typically, machined parts (produced on CNC mills or lathes) are measured using large machines known as coordinate measuring machines. Measuring parts using the camera system presented here has the potential to greatly reduce the number of parts which are scrapped when something goes wrong with one of the production machines. This is due to the removal of the delay between a fault occurring and the diagnosis of that fault, a delay during which more faulty parts would have been produced. Building the system required extensive mechanical, electronics, and software design work.

Preface

This thesis is the original, unpublished work of the author, Eric Buckley.

Dr. Xiaodong Lu provided me with significant guidance in all aspects of the camera system design and the research program. A portion of the FPGA logic used in the cameras was the original work of Niankun Rao and Dr. Xiaodong Lu.

Table of Contents

List of Tables

List of Figures

Acknowledgements

I would like to thank Dr. Xiadong Lu and Professor Yusuf Altintas for their guidance and supervision during this project. Dr. Lu’s enthusiasm for mechanical and electronic design was inspiring. Professor Altintas’ insight into production machining processes was invaluable to this work.

Thanks are also due to the Boeing Company, the NSERC Canadian Network for Research and Innovation in Machining Technology, and the NSERC Canada Graduate Scholarships Program for providing funding for this project.

Dedication

To all my friends and family who told me to “just get it done”.

Chapter 1: Introduction

Metrology systems are a crucial part of any manufacturing operation. They provide much needed information for quality control and process monitoring. In the case of a coordinate measurement machine used for part checking, there are criteria beyond the dimensional accuracy and precision of the system which determine its value. Gantry CMMs are used for many complex part inspections due to their very high accuracy. The downside to inspection with a gantry CMM is that it requires parts to be removed from the machines on which they were cut, moved to the CMM, and fixed to the measurement platform on the CMM. This process requires time and floor space in the shop, and leads to a delay between the production and detection of defective parts. All of these add significantly to the cost of production. A measurement tool which would allow early detection of defective parts, while occupying little floor space and requiring little time to use, would therefore be very valuable to a manufacturing facility which must meet strict quality control standards. This thesis will demonstrate that an optical CMM can be constructed which could be installed on the production machines and used to quickly inspect parts as they are produced.

The proposed system uses cameras with CMOS image sensors to track three or more (such as four) infra-red LED targets on a handheld probe at high speed. Two cameras are fixed to a frame which keeps their positions constant. From the measurement of the LED image positions on the cameras sensors, the 3D position of each target can be triangulated. Once the positions of at least three targets are known, the position and orientation of the probe are known and can be used to calculate the location of the probe tip center. This system allows the operator to use a handheld probe to make point measurements on the surface of a part and further to derive dimensional information of geometric features.

1.1 Comparable Measurement Devices

There are a number of devices available which can be used for fast and flexible coordinate measurement. These devices typically fall into a few broad categories: optical CMMs, laser trackers, and probing arms.

1.1.1 AICON MoveInspect

AICON 3D systems GmbH makes a series of optical CMMs with the name MoveInspect. These systems are tuned for different applications. The MoveInspect HR is the high resolution system. It uses 5MP cameras to provide measurements at 30Hz, and an accuracy of 20μm in a $1m^3$ measurement volume [1]. For applications requiring a larger measurement volume, the cameras must be attached to independent tripods. This configuration significantly reduces accuracy since the cameras can easily move relative to one another [2]. The slow measurement frequency of the MoveInspect probing systems means that there is not the opportunity to average many measurements to reduce random noise.

1.1.2 Creaform HandyProbe

The HandyProbe is an optical CMM using two cameras to track a handheld probe with retro-reflective targets. The system is able to provide measurements at a frequency of 80Hz, and with an accuracy of 20 μm for a calibrated spherical artifact [3]. The system's accuracy is reduced to 80 μm in a large measurement volume of $16m^3$. Due to its single piece construction, the camera system used by the HandyProbe is not able to be reconfigured for different applications.

1.1.3 Leica Absolute Tracker

The Leica Absolute Tracker uses a laser interferometer and a pair of rotary encoders to measure the position of a handheld target probe. It is able to measure with accuracy of 50 μm + 6 μm/m of distance between the tracker and the probe. Previous laser trackers have had difficulties recovering from obscured targets since they performed incremental measurements, however Leica seems to have overcome these difficulties by using an “absolute interferometer”. This may be an interferometer using multiple frequencies to eliminate the uncertainty in the number of wavelength increments, as described in [4]. One downside to interferometric measurements is that they are linearly dependent on the index of refraction of the medium through which the laser travels. There can be significant variations of the index of refraction of air with temperature, pressure, and moisture content.

1.1.4 FaroArm

The FaroArm is a portable CMM which uses a multi-jointed arm to connect the handheld probe to the fixed base. The joints of the arm are equipped with encoders which allow the relative orientations of all of the arm segments to be measured and used to calculate the position of the probe tip. The FaroArm provides single point repeatability of up to 24 µm, and a spherical working volume with a radius of up to 3.7m [5]. The accuracy of the FaroArm is dependent on the strain on the arm segments. Temperature changes will cause expansion and contraction along the length of the segments, while changing orientation will cause bending in different directions. The FaroArm includes temperature sensors to compensate for some of the thermal expansion error.

1.2 State of the Art of Photogrammetry

1.2.1 Bundle Adjustment (Offline) Reconstruction Methods

Offline bundle adjustment reconstruction methods are used for object measurement in a variety of applications, from alignment of parts during automotive and aircraft assembly to telescope construction [6] and . They allow a very simple system to be used for measurement, often as little as an off the shelf handheld camera and some retro-reflective targets [7]. Offline systems can also be very flexible since the camera can be moved to positions which are convenient for each different part or location. Because bundle adjustment methods are able to use very flexible network topologies and optimize all parameters at once, including the unknown object points, they provide the highest precision and accuracy. Luhmann [7] finds that offline systems using digital cameras provide measurement precision (rms 1-sigma) of approximately 1:100,000 in relation to the longest dimension of the object being measured. This depends on sub-pixel target interpolation algorithms which can locate a control point in the image with a precision of 1/50 of a pixel. Luhmann also notes that large format analogue reseau cameras, when used with digital image scanning and processing systems are able to achieve significantly better precision, up to 1:500,000. The downside to offline reconstruction methods is that they are slow, making them impractical in applications where immediate information is needed or where some of the components to be measured are not stable.

1.2.2 Real-Time (Online) Reconstruction Methods

Online reconstruction methods integrate a computer with the cameras in order to generate measurement data in real-time. In a dimension checking application, this allows an operator to immediately determine whether a part is within spec or not. More generally, feedback to the operator is useful in ensuring that measurements are performed correctly since problems such as obscured targets or incorrect camera settings will be immediately obvious, saving time and the effort of repeating measurements. Online reconstruction methods are usually less accurate than offline methods, often achieving accuracy of between 1:10,000 and 1:4,000 [7] [8]. Luhmann [7] attributes the lower performance of online reconstruction methods to:

- Fewer target images used per measurement
- Restricted placement of the cameras to suboptimal locations
- Less flexible camera calibration
- Manual operation of probes or target objects

With fewer images, an online system is less able to average out random error in measurements. This can be overcome with a higher frequency system which can average measurements as they are produced, however the system frequency must be high enough that this does not cause a noticeable delay to the user. The acceptable delay will depend on the exact circumstances under which the system is used.

Most online systems use a fixed frame, keeping the relationship between the cameras constant. This is necessary since the system must be calibrated prior to use, and the system parameters can't change between calibration and measurement if the system is to remain accurate. A fixed frame hampers the system by forcing the use of suboptimal camera locations and orientations. Ideally, camera positions and would be selected to have the measurement object occupy all of the measurement volume, where the camera views overlap, and the cameras would be oriented so that their views converge on the measurement object. This provides the highest accuracy measurement by using the full range of the image sensors. A system using a fixed frame cannot provide the best camera positions for all applications, and therefore provides lower accuracy.

The flexibility of camera calibration methods, and camera models for online reconstruction, can also limit the performance of online systems. Since reconstruction must be done in real-time, the camera model must not be too computationally intense. In most cases this means that the model should not require an iterative calculation during reconstruction. This requires some models of lens distortion to be linearized [9] [10] [11]. The inability to adjust model parameters from image to image means that any movement in the system cannot be compensated after calibration. This can be a significant problem if cameras are not designed with this mechanical constraint in mind, as the sensor and lens can move relative to one another [12].

Manual operation of probes can compromise accuracy in a number of ways. It is inevitable that operators will apply inconsistent forces to the probe and the test piece during measurement, causing corresponding deflection and measurement error. Contact of the operator’s hands with different parts of the test piece and the probe may cause inconsistent heating of these and corresponding expansion. Operators may not orient probes optimally, reducing the signal measured by the cameras, obscuring targets from view, etc.

While systems using on-line reconstruction methods usually provide lower accuracy than off-line systems, this effect can be mitigated in a number of ways. A camera model which incorporates sufficient terms for non-linear distortion is able to quite accurately model the behavior of cameras. A system which has a high measurement frequency can provide multiple images for each measurement, averaging out random error. The ability to reconfigure the system to have different camera positions and orientations allows for the optimization of camera position for different measurement tasks.

1.2.3 Camera Model

The camera model mathematically describes the camera’s transformation of points in 3D space (world coordinates) into points on the image sensor (pixel coordinates). Rao [10] compared the performance of a number of camera calibration models. He found that a model which includes two parameters for radial distortion and tangential distortion provides an appropriate balance of complexity and performance. The model starts with a coordinate transformation (rotation and translation) from world coordinates to camera coordinates:

$$\begin{bmatrix} x_c \\ y_c \\ z_c \\ 1 \end{bmatrix} = \begin{bmatrix} R_{11} & R_{12} & R_{13} & x_0 \\ R_{21} & R_{22} & R_{23} & y_0 \\ R_{31} & R_{32} & R_{33} & z_0 \\ 0 & 0 & 0 & 1 \end{bmatrix} \begin{bmatrix} X_w \\ Y_w \\ Z_w \\ 1 \end{bmatrix}$$

The rotation can be considered as a series of three rotations of the coordinate system using the Tait-Bryan angle convention. First, a rotation of α around the x-axis of the world coordinate system, then a rotation of β about the intermediate y-axis, and finally a rotation of γ about the z-axis of the rotated coordinate system whose orientation matches that of the camera coordinate system:

$$\boldsymbol{R} = \boldsymbol{R_z R_y R_x}$$

$$\boldsymbol{R} = \begin{bmatrix} cos\gamma & sin\gamma & 0 \\ -sin\gamma & cos\gamma & 0 \\ 0 & 0 & 1 \end{bmatrix} \begin{bmatrix} cos\beta & 0 & -sin\beta \\ 0 & 1 & 0 \\ sin\beta & 0 & cos\beta \end{bmatrix} \begin{bmatrix} 1 & 0 & 0 \\ 0 & cos\alpha & sin\alpha \\ 0 & -sin\alpha & cos\alpha \end{bmatrix}$$

The translation vector is the distance from the origin of the camera coordinate system to the origin of the world coordinate system in camera coordinates.

After the coordinate transformation, the point in camera coordinates is projected onto the image sensor plane using a pinhole model:

$$\begin{bmatrix} x_i \\ y_i \end{bmatrix} = \frac{f}{z_c} \begin{bmatrix} x_c \\ y_c \end{bmatrix}$$

Where f is the focal length of the lens.

The full equations for the ideal target image position as functions of the target position in world coordinates are:

$$x_i = f \frac{R_{11} X_w + R_{12} Y_w + R_{13} Z_w + x_0}{R_{31} X_w + R_{32} Y_w + R_{33} Z_w + z_0}$$

$$y_i = f\frac{R_{21}X_w + R_{22}Y_w + R_{23}Z_w + y_0}{R_{31}X_w + R_{32}Y_w + R_{33}Z_w + z_0}$$

At this point the corrections for radial and tangential distortion are applied to the pinhole projection. The radial distortion is:

$$\delta x_{i,rad} = x_i(k_1({x_i}^2 + {y_i}^2) + k_2({x_i}^2 + {y_i}^2)^2)$$

$$\delta y_{i,rad} = y_i(k_1({x_i}^2 + {y_i}^2) + k_2({x_i}^2 + {y_i}^2)^2)$$

The tangential distortion is:

$$\delta x_{i,tan} = 2p_1 x_i y_i + p_2(3{x_i}^2 + {y_i}^2)$$

$$\delta y_{i,tan} = p_1({x_i}^2 + 3{y_i}^2) + 2p_2 x_i y_i$$

The image point is then transformed from the image plane coordinates to the digital pixel coordinates, allowing for different pixel scales in the x and y axes and an offset from the center of the image plane to the origin of the image sensor.

$$\begin{bmatrix} u_i \\ v_i \end{bmatrix} = \begin{bmatrix} S_x(x_i + \delta x_{i,rad} + \delta x_{i,tan}) \\ S_y(y_i + \delta y_{i,rad} + \delta y_{i,tan}) \end{bmatrix} + \begin{bmatrix} u_0 \\ v_0 \end{bmatrix}$$

1.3 Literature Relating to the Probe Calibration and Tip Position Reconstruction

The geometry of the probe will be determined using data collected with the camera network. Algorithms for this were not found in my review of the literature, however there are a number of documented tools which can be combined to achieve the calibration. The calibration problem can be broken down into two steps:

- Determining the position of the probe ball center in the world coordinate system
- Measuring the positions of the LED targets relative to the probe ball center

The first step is achieved by rotating the probe through a number of positions with the probe ball held stationary. The LED targets are thereby made to trace arcs about the center of the probe ball. Spheres are fit to these arcs and the centers of these spheres indicate the position of the probe ball center.

Once the location of the probe ball center is known, the positions of the LEDs relative to the probe ball center can be taken from any of the measurements used in the sphere fitting. In order to get a better measurement for the calibration it is beneficial to take the average of all of the measurements collected in the first step. Since the measurements are all taken with the probe in different orientations, it is necessary to rotate them to the same orientation before averaging. This is done using a Procrustes method. The same Procrustes method is also used for probe tip position reconstruction when the system is in operation,

1.3.1 Sphere Fitting Methods

By rotating the probe body about the center of the probe ball, a number of target locations can be collected which are on the surface of a sphere whose center is the location of the probe ball center. Finding this location is then a matter of fitting a sphere to the points. A number of methods have been described which fit circles to data points in 2 dimensions [13] [14] [15]. These methods can be extended to fit spheres to points in 3 dimensions.

1.3.1.1 2D Circle Fitting Linear Least Squares Method

As described by Umbach & Jones [13], Coope [14], and Kasa [15], a linear least squares method can be used to fit a circle to a set of points when the minimization criterion is altered slightly. While the typical criterion would be to minimize the square of the distance of each data point from the surface of the sphere:

$$min \sum_{i=1}^{n} [r - \sqrt{(x_i - a)^2 - (y_i - b)^2}]^2 = SS$$

Where the center of the best fit circle is at (a, b) and its radius is r. Changing the criterion to:

$$min \sum_{i=1}^{n} [r^2 - (x_i - a)^2 - (y_i - b)^2]^2 = SS$$

Allows a minimization problem to be constructed as follows:

$$\frac{\partial SS}{\partial r} = 4r \sum_{i=1}^{n} [r^2 - (x_i - a)^2 - (y_i - b)^2] = 0$$

$$\frac{\partial SS}{\partial a} = -4 \sum_{i=1}^{n} \{[r^2 - (x_i - a)^2 - (y_i - b)^2] * (x_i - a)\} = 0$$

$$\frac{\partial SS}{\partial b} = -4 \sum_{i=1}^{n} \{[r^2 - (x_i - a)^2 - (y_i - b)^2] * (y_i - b)\} = 0$$

These can be simplified to:

$$\sum_{i=1}^{n} [r^2 - (x_i - a)^2 - (y_i - b)^2] = 0$$

$$\sum_{i=1}^{n} \{[r^2 - (x_i - a)^2 - (y_i - b)^2] * x_i\} = 0$$

$$\sum_{i=1}^{n} \{[r^2 - (x_i - a)^2 - (y_i - b)^2] * y_i\} = 0$$

as long as $r \neq 0$, and there are some $x_i \neq a$, and $y_i \neq b$. These can, in turn, be rewritten as:

$$n * (r^2 - a^2 - b^2) + \sum_{i=1}^{n} (2ax_i + 2by_i) = \sum_{i=1}^{n} ({x_i}^2 + {y_i}^2)$$

$$\sum_{i=1}^{n} [(r^2 - a^2 - b^2)x_i + 2a{x_i}^2 + 2by_ix_i] = \sum_{i=1}^{n} ({x_i}^3 + {y_i}^2x_i)$$

$$\sum_{i=1}^{n} [(r^2 - a^2 - b^2)y_i + 2ax_iy_i + 2b{y_i}^2] = \sum_{i=1}^{n} ({x_i}^2y_i + {y_i}^3)$$

Which forms a linear system of 3 equations with three unknowns if $(r^2 - a^2 - b^2)$ is considered to be the third unknown variable.

1.3.1.2 Extension to 3D Sphere Fitting

In the case where a sphere must be fit to a set of three-dimensional points, the error criterion to be minimized is:

$$min\sum_{i=1}^{n}[r^2 - (x_i - a)^2 - (y_i - b)^2 - (z_i - c)^2]^2 = SS$$

And the partial derivatives are:

$$\frac{\partial SS}{\partial r} = 4r\sum_{i=1}^{n}[r^2 - (x_i - a)^2 - (y_i - b)^2 - (z_i - c)^2] = 0$$

$$\frac{\partial SS}{\partial a} = -4\sum_{i=1}^{n}\{[r^2 - (x_i - a)^2 - (y_i - b)^2 - (z_i - c)^2] * (x_i - a)\} = 0$$

$$\frac{\partial SS}{\partial b} = -4\sum_{i=1}^{n}\{[r^2 - (x_i - a)^2 - (y_i - b)^2 - (z_i - c)^2] * (y_i - b)\} = 0$$

$$\frac{\partial SS}{\partial c} = -4\sum_{i=1}^{n}\{[r^2 - (x_i - a)^2 - (y_i - b)^2 - (z_i - c)^2] * (z_i - c)\} = 0$$

Which simplify to:

$$\sum_{i=1}^{n}[r^2 - (x_i - a)^2 - (y_i - b)^2 - (z_i - c)^2] = 0$$

$$\sum_{i=1}^{n}\{[r^2 - (x_i - a)^2 - (y_i - b)^2 - (z_i - c)^2] * x_i\} = 0$$

$$\sum_{i=1}^{n}\{[r^2 - (x_i - a)^2 - (y_i - b)^2 - (z_i - c)^2] * y_i\} = 0$$

$$\sum_{i=1}^{n}\{[r^2 - (x_i - a)^2 - (y_i - b)^2 - (z_i - c)^2] * z_i\} = 0$$

Again, provided $r \neq 0$, $x_i \neq a$, $y_i \neq b$, and $z_i \neq c$. The system of equations can be written as:

$$n * (r^2 - a^2 - b^2 - c^2) + \sum_{i=1}^{n}(2ax_i + 2by_i + 2cz_i) = \sum_{i=1}^{n}({x_i}^2 + {y_i}^2 + {z_i}^2)$$

$$\sum_{i=1}^{n}[(r^2 - a^2 - b^2 - c^2)x_i + 2a{x_i}^2 + 2by_ix_i + 2cz_ix_i] = \sum_{i=1}^{n}({x_i}^3 + {y_i}^2x_i + {z_i}^2x_i)$$

$$\sum_{i=1}^{n}[(r^2 - a^2 - b^2 - c^2)y_i + 2ax_iy_i + 2b{y_i}^2 + 2cz_iy_i] = \sum_{i=1}^{n}({x_i}^2y_i + {y_i}^3 + {z_i}^2y_i)$$

$$\sum_{i=1}^{n}[(r^2 - a^2 - b^2 - c^2)z_i + 2ax_iz_i + 2by_iz_i + 2c{z_i}^2] = \sum_{i=1}^{n}({x_i}^2z_i + {y_i}^2z_i + {z_i}^3)$$

This time the fourth unknown is $(r^2 - a^2 - b^2 - c^2)$. This system of equations can be written in matrix form as:

$$\boldsymbol{A} = \begin{bmatrix} 2\Sigma x_i & 2\Sigma y_i & 2\Sigma z_i & n \\ 2\Sigma {x_i}^2 & 2\Sigma y_ix_i & 2\Sigma z_ix_i & \Sigma x_i \\ 2\Sigma x_iy_i & 2\Sigma {y_i}^2 & 2\Sigma z_iy_i & \Sigma y_i \\ 2\Sigma x_iz_i & 2\Sigma y_iz_i & 2\Sigma {z_i}^2 & \Sigma z_i \end{bmatrix}$$

$$\boldsymbol{x} = \begin{bmatrix} a \\ b \\ c \\ r^2 - a^2 - b^2 - c^2 \end{bmatrix}$$

$$\boldsymbol{b} = \begin{bmatrix} \Sigma {x_i}^2 + \Sigma {y_i}^2 + \Sigma {z_i}^2 \\ \Sigma {x_i}^3 + \Sigma {y_i}^2x_i + \Sigma {z_i}^2x_i \\ \Sigma {x_i}^2y_i + \Sigma {y_i}^3 + \Sigma {z_i}^2y_i \\ \Sigma {x_i}^2z_i + \Sigma {y_i}^2z_i + \Sigma {z_i}^3 \end{bmatrix}$$

$$\boldsymbol{Ax} = \boldsymbol{b}$$

And x can be solved by:

$$\boldsymbol{x} = \boldsymbol{A}^{-1}\boldsymbol{b}$$

1.3.2 Procrustes Analysis

Once the fifth point is known, the probe geometry is known. However, the problem of determining the ball center location during measurement still remains. In this case it will not be practical to rotate the probe body about the tip center, so another method is needed. What is needed is to determine the translation and rotation of the probe body from the calibrated position to the measured position. Once this coordinate transformation is known, it can be applied to the calibrated ball center location to get the measured ball center location. The problem of finding a transformation which best fits one set of coordinates to another set is referred to as a Procrustes problem. Gower and Dijksterhuis [16] present solutions to these in their book "Procrustes Problems". In our case it is necessary to restrict the transformation so that no scaling or reflection operations are included in the solution. Gower & Dijksterhuis refer to this as an orthogonal Procrustes problem since the transformation matrix relating the two sets of coordinates must be orthogonal. Gower and Dijksterhuis give the following method to calculate the transformation $\boldsymbol{Q}$ which best fits one set of points to another, transformed, set by the criterion:

$$min\sum_{i=1}^{N}[(x_{1i} - x_{ti})^2 + (y_{1i} - y_{ti})^2 + (z_{1i} - z_{ti})^2]$$

If the set of transformed coordinates is represented as a matrix:

$$\begin{bmatrix} x_{t1} & y_{t1} & z_{t1} \\ \vdots & \vdots & \vdots \\ x_{tN} & y_{tN} & z_{tN} \end{bmatrix} = \boldsymbol{X_2Q}$$

The criterion can be written as:

$$min \,\|\boldsymbol{X_1} - \boldsymbol{X_2 Q}\|$$

Gower and Dijksterhuis demonstrate that $\boldsymbol{Q}$ can be found by expressing $\boldsymbol{X_1}'\boldsymbol{X_2}$ as its singular value decomposition:

$$\boldsymbol{X_1}'\boldsymbol{X_2} = \boldsymbol{U\Sigma V}'$$

And setting

$$\boldsymbol{Q} = \boldsymbol{VU}'$$

The residual sum of squares is then:

$$\|\boldsymbol{X_1} - \boldsymbol{X_2 Q}\| = \|\boldsymbol{X_1}\| + \|\boldsymbol{X_2}\| - 2trace(\boldsymbol{\Sigma})$$

Where $trace(\boldsymbol{\Sigma})$ is the sum of its diagonal, and only non-zero entries.

Gower and Dijksterhuis also present an algorithm for fitting a large group of point sets to each other to find the group average. For K sets of data, the group average is:

$$\boldsymbol{G} = \frac{1}{K}\sum_{j=1}^{K} \boldsymbol{X}_j \boldsymbol{Q_j}$$

The algorithm works iteratively, fitting each data set $\boldsymbol{X_j}$ to the previous estimate of $\boldsymbol{G}$ to calculate the current value of $\boldsymbol{Q_j}$. When all $\boldsymbol{Q_j}$ have been calculated, they are used to update the group average. At the start of the algorithm, the first data set $\boldsymbol{X_1}$ is used as an estimate of the group average .

1.4 Structure of the Thesis

In the first chapter, I have reviewed the state of the art of dimension checking and coordinate measuring machines. The literature pertaining to photogrammetry systems has been reviewed, as well as the mathematical tools needed to perform the calibration and position reconstruction used in the system described in this thesis. The remainder of the thesis is organized into three chapters as follows:

- Chapter 2: Design of the Optical Coordinate Measuring Machine

  This includes the selection of optical and electronic components for the probe and cameras; the design of the electronic circuits for the cameras; the mechanical design of the probe, cameras and frame; and the software system and algorithm design.

- Chapter 3: Calibrating and Testing the Optical Coordinate Measuring Machine

  This chapter describes the calibration processes for the camera network and the handheld probe. The camera calibration is necessary to determine the unknown geometric and lens distortion properties of the camera network. The calibration process uses a Mitutoyo Coordinate Measuring Machine (CMM) to move an LED target to a series of known locations while the cameras capture images of the target. The probe calibration is necessary to determine the locations of the LED targets relative to the probe ball center. This is done using only data collected by the camera network while the probe is rotated about the ball center.

  The performance of the system is evaluated in three ways. First, the accuracy of the camera calibration is assessed by comparing a series of target position measurements made with the cameras to the CMM measurements of these positions. The accuracy of the probe calibration is assessed using a simulation and by observing the residual error in the calibration process. Finally a series of probing measurements are performed on two reference objects: a CMM calibration ball of known diameter and a flat plate. These are used to demonstrate the overall accuracy of the system.

- Chapter 4: Conclusion

The conclusion discusses the benefits of the proposed optical coordinate measuring machine. The performance is compared to that of other optical measurement systems.

Chapter 2: Design of the Optical Coordinate Measuring Machine

The goal in designing this optical measurement system is to provide the most accurate measurement possible of the location of the probing tip of a handheld probe while making the system flexible enough to provide accurate measurements in various applications.

2.1 System Overview

The proposed metrology system uses a series of cameras to track infrared (IR) LED targets on a handheld probe. This allows the position and orientation, or pose, of the probe to be measured from which the location of the probe's tip can be determined. The ability to accurately measure the location of the probe's tip in real-time allows the probe to replace typical dimension measurement machines in dimension checking applications.

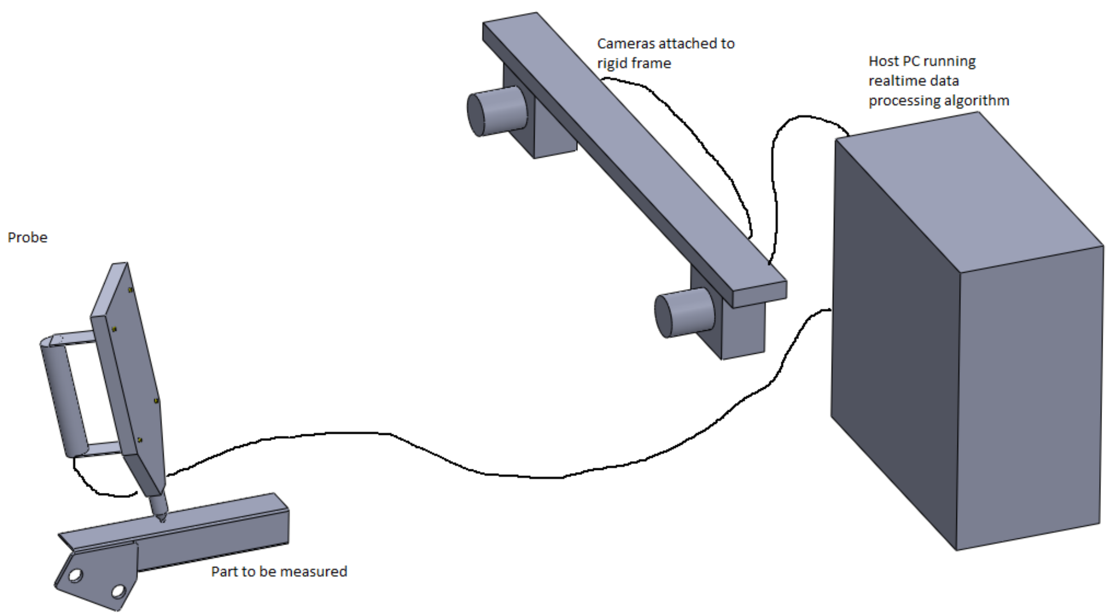

Figure 1: Diagram of the optical metrology system

The minimum configuration for measurement requires two cameras and three LED targets on the probe. Each camera is able to measure the position of the LED target images on its image sensor.

Each 2D image position defines a line, projecting from the lens, on which the target lies. The cameras transmit this 2D target image position data to the host PC (real-time computer). In the ideal case the position of a target in 3D is at the intersection of the lines projecting from the two cameras. Since there is some error in measurement, the position reconstruction algorithm on the host PC calculates the point at which the lines come closest to intersecting. Once the positions of 3 LED targets are calculated, the algorithm is able to calculate the location of the probe tip. This location is then sent to the Polyworks dimension checking software where it can be compared to a model of the part being tested.

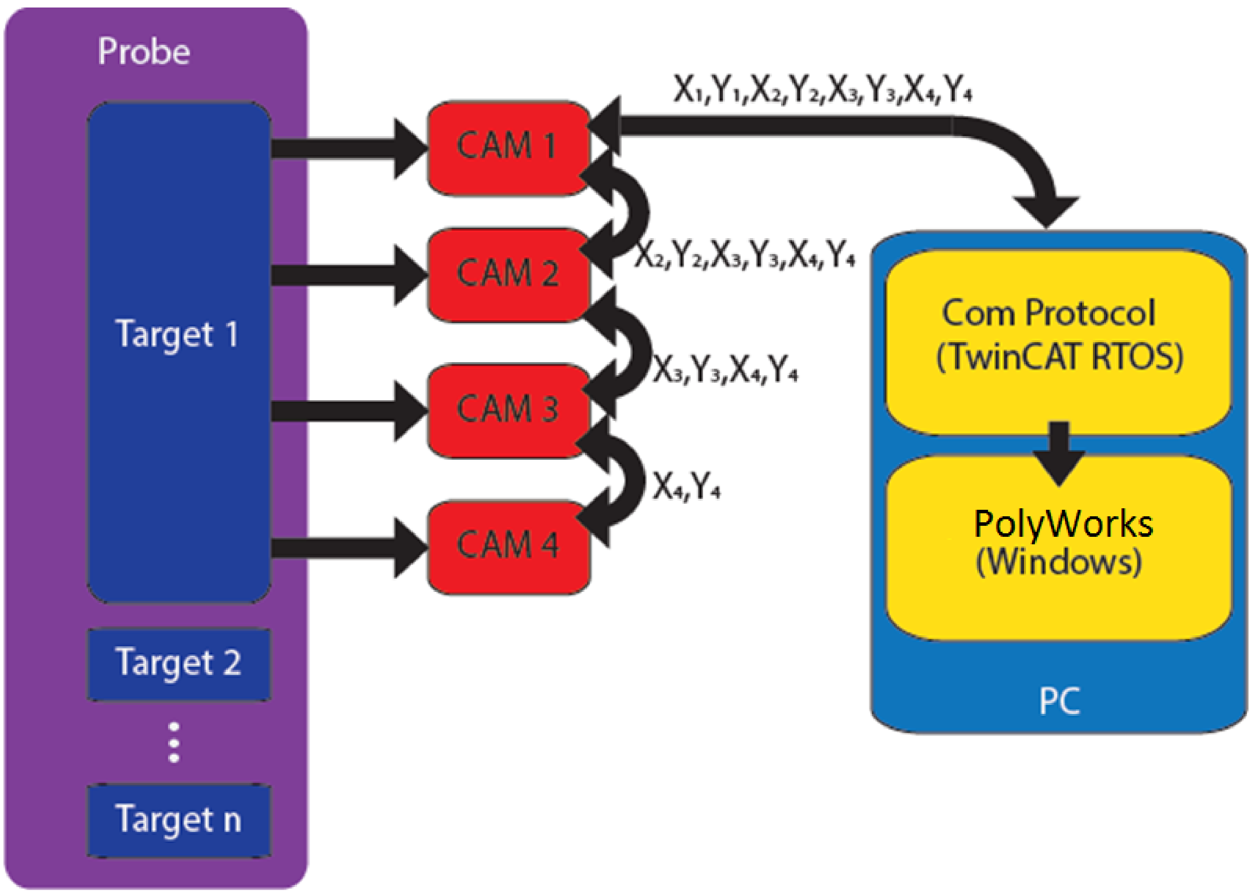

Figure 2: Block Diagram of the proposed system showing the flow of information in the measurement process

Adding additional targets to the probe and measuring using more than two cameras can reduce the error in measurement by averaging as well as provide redundancy in measurement situations where some targets may be occluded. The system hardware and software are designed to allow a flexible number of cameras and targets to be tracked. However, tracking more than 8 LEDs with each camera will slow down the measurement frequency of the system.

2.2 High Speed Target Tracking Camera Design

The target tracking camera is the most complex part of the optical CMM. It must capture the image of the LED targets, calculate the location coordinates of the centroid of the target image, and transmit this coordinate information to the real-time computer. The accuracy of the system depends on the ability of the camera to quickly capture consistent, high resolution images in very tight synchronization with the other cameras in the system, while maintaining the position of the lens and image sensor constant relative to each other and relative to the other cameras as well.

2.2.1 Image Sensor Selection

There are a number of factors which direct the choice of an image sensor. The image sensor should have a large area (~ full frame size or larger) so that it may use high quality, commercially available lenses. It should have a high resolution and high dynamic range to increase the system’s measurement resolution. It should have a high frame rate, as this will most likely be the factor which limits the system’s measurement frequency and latency. It should also support a global shutter operation, where all pixels are exposed simultaneously, so that the targets cannot move relative to one another during the exposure. In order to find the best image sensor for the application, a survey of available image sensors was done. Only CMOS image sensors were considered, since they support windowing to increase the frame rate. The most likely candidate sensors are compared in the following section. While there are a number of sensors which offer high resolution, high dynamic range, large frame sizes, and high speed data outputs, most do not provide the windowing flexibility needed to excel in this specific application.

2.2.1.1 CMOSIS CMV12000 and CMV20000

CMOSIS Image Sensors produces two high resolution sensors with large frame sizes, the CMV12000 (12 MP) and the CMV20000 (20 MP). The CMV12000 sensor has a frame size of 22.5 mm x 16.9 mm [17], while the CMV20000 is a full 35 mm x 26 mm [18]. Both sensors support global shutter operation. They have dynamic ranges of 60 dB for the CMV12000 and 66 dB for the CMV20000. The sensors have multiple built in ADCs to which the pixel outputs are multiplexed. The ADCs are assigned to read signals from certain columns only. This "column ADC" layout means these sensors are only able to achieve higher frame rates by windowing in the Y-direction, not both X and Y, since all of the columns are read out in parallel [19]. The result is that, despite high frame rates when reading the whole sensor, the CMV12000 and CMV20000 are only able to operate at 1300 fps and 870 fps, respectively, when reading out 8 windows with heights of 20 pixels.

2.2.1.2 viimagic 9225

The viimagic 9225 is a high speed sensor with a smaller optical format. It has a frame size of 10.3mm x 5.5mm, a resolution of 2MP, and a dynamic range of 60dB. The sensor has 4 built in ADCs with 12bit resolution. Windowing is possible with the viimagic 9225, however it does not allow for a large number of independent regions of interest to be read out so it would need to be operated in full frame mode if it were used in the target tracking camera. In full frame mode, the sensor can operate at 240 frames per second.

2.2.1.3 Alexima AM41V4

The AM41V4 is a high speed sensor designed for machine vision and inspection applications. It has a resolution of 4 MP (2336 x 1728), with a frame size of 16.4 mm x 12.1 mm. A dynamic range specification is not listed, however the built in ADCs have a 10 bit resolution so we can assume that the dynamic range is less than 60 dB, likely significantly less. The built in ADCs are connected to individual columns of pixels, so the frame rate can only be sped up by windowing in the Y-direction. When reading 8 windows with heights of 20 pixels, the sensor can operate at almost 4000 frames per second.

2.2.1.4 ON Semi NOILSM4000A (LUPA4000)

The NOILSM4000A is a 4MP (2048 x 2048) sensor designed for machine vision applications. It has a dynamic range of 66 dB. The sensor outputs the pixel values as analog voltage signals which are to be converted to digital values with an external ADC. This allows for very high accuracy ADCs to be used, at the cost of low pixel throughput. When reading out the full frame, the sensor can only operate at 15 fps, however it is able to speed up the readout by windowing in both the X and Y directions so that it can operate at 8300 fps when reading 8 windows of 20 x 20 pixels.

2.2.1.5 Sensor Topology: On-Chip vs. Off-Chip AD Conversion

The trend in image sensor design seems to be towards greater integration of functionality into the sensor chip. This provides many benefits to the users of image sensors: shorter development times, higher speeds (since signals must cover shorter distances), less interference from other circuitry on the board. The downside which we see in the comparison of available sensors is that this architecture severely limits the ability of a sensor user to achieve speedup by windowing to small regions of interest.

2.2.2 Sensor Control and Image Processing Electronics

The chosen image sensor can operate at a pixel rate of up to 33MHz. To control the sensor, a number of signals must be supplied. These range in frequency up to the pixel frequency. In order to get the maximum available performance from the sensor, it is necessary to interface it with hardware that can supply the required control signals at the maximum frequency supported by the sensor as well as read its' data output at this rate. Since the control interface is fast and is not a standard or widely used protocol, it is not possible to use a microcontroller, and an FPGA is the most practical device to be used. A Spartan 6 LX100 FPGA was selected since it supports clock and IO frequencies greater than 300MHz and provides a large number of logic blocks so that the control and image processing logic can be developed without worrying about exceeding the capacity of the FPGA. Since the Spartan 6 has only digital inputs and outputs, a separate analog to digital converter (ADC) is needed to read the analog pixel values from the image sensor.

2.2.3 Analog to Digital Converter

As with the FPGA, the ADC must be able to operate at frequencies at least as high as the sensor's pixel frequency. The other criterion used to select the ADC is its' precision. The image sensor's dynamic range is 66dB [20]. This can be translated into a precision in bits:

$$bits = \frac{DR}{20\log(2)} = \frac{66dB}{20\log(2)} \cong 11$$

It is desirable to keep the quantization error of the ADC to a level which is insignificant compared to the noise already present in the system. This requires the ADC to have a precision significantly higher than the image sensor, ideally by an order of magnitude. An ADC with 14-

bit precision gets quite close to this, providing precision approximately 8 times better than the image sensor.

2.2.4 Memory

Due to the large variation in pixel to pixel dark signal from the image sensor, it is desirable to perform a black image correction which subtracts a stored black pixel value from the pixel value measured when the image is collected. In order to do this, two types of memory are used. Two 8 MB chips of non-volatile flash memory are used to store the black image data when the camera is powered off. These are not fast enough to stream the black image data back to the FPGA while the image is captured, so a faster, volatile, DDR memory chip is used to stream the data while the camera is in operation. In addition to streaming the black image data to the FPGA during image readout and processing, the high speed of the DDR memory allows snapshots to be captured of the image sensor data while the camera is running, and allows flexibility for future additions to the image processing algorithms implemented on the camera.

2.2.5 Communication Interface

The communication interface must collect data from multiple cameras and transmit this data to a real-time computer where the target position reconstruction can be performed using the image coordinate data from the individual cameras. The system must be able to transmit the coordinates for each camera at the frame rate of the system, so it must support a sufficient bandwidth. It is also important for all of the cameras to capture their images synchronously to avoid errors from target movement between the different images. Since optical coordinate measurement systems may need to be used in different settings, for example: different machines with different measurement volumes and line of sight obstructions, it is desirable to have a system which provides the maximum possible flexibility in terms of the number and location of the cameras. A number of potential communication interfaces were considered for the system. The EtherCat interface was selected because supports a bandwidth of up to 100 Mbps, and allows synchronization of the slave devices to within 20 ns of each other [21]. It has the added benefit of easy integration into the TwinCAT real-time operating system.

2.2.6 Electronic Circuit Board Design

Careful design of the circuit boards for the camera is necessary to ensure that the system operates to its potential. The analog components of the circuit, the image sensor pixel supplies and outputs, the differential amplifiers and the ADC inputs, must be separated from the digital components in order to minimize the noise that is introduced to the pixel signals before they can be digitized. The image sensor has strict requirements for power supply levels which must be met to ensure that it performs well. The volatile memory interface and the Ethernet interface both operate at very high speeds, so the layout of their signal traces required the consideration of timing and termination requirements to ensure that good signal integrity was maintained.

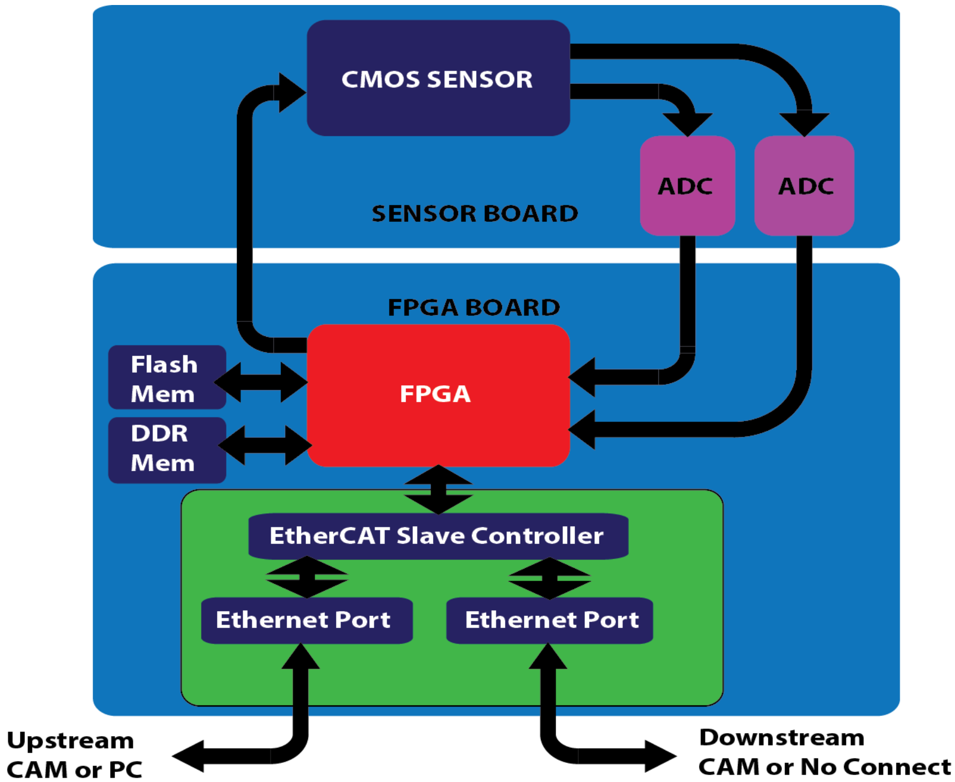

Figure 3: Block Diagram of the Measurement Camera Electronics

Separation of the analog and digital components of the circuit was achieved by placing the image sensor and associated analog circuitry on one board, the Sensor Board, and placing the bulk of the digital circuits on a second board, the FPGA Board. This immediately separates the noisiest components, those switching large voltages or currents at high speeds [22], from the most sensitive components, those trying to transmit and measure very small variations in voltage. On the Sensor Board, there are still digital signals which are necessary for controlling the sensor, the ADC and other peripheral chips as well as transmitting the ADC data to the FPGA board. Therefore there is still a region of the sensor board which is considered to belong to the digital part of the circuit and must be kept separate. All of the digital signal traces and power supply planes must be placed in this digital region.

Power to the sensor must be supplied with seven different regulators in order to meet the supply voltage and current requirements and to keep sensitive modules isolated from each other [20].

2.2.7 Lens Selection

A number of concerns govern the selection of an appropriate lens for the camera. The field of view of the lens is an important factor governing the size and location of the system's working volume. The optical materials and coatings of the lens will determine whether it is suitable for imaging the targets used by the system. The distortion characteristics of the lens must match the form of the compensation which is applied in the camera calibration model. Finally, the lens must be solidly constructed and stiffly attached to the camera body so that it does not move relative to the lens under the force of gravity when positioned in different orientations or during any vibration which the system may experience during use.

The selection of the lens focal length determines the field of view of the camera, and therefore the size, shape, and position of the system's working volume relative to the cameras. The selection of a lens with a long focal length allows for better precision in a small measurement volume, or in a location far from the cameras, while a lens with a short focal length gives a wider view angle and therefore allows the system to have a large measurement volume located close to the cameras.

If there is no requirement to have the measurement volume far away from the cameras it is preferable to have it as close as possible. This minimizes the path that the light travels from the target to the camera and thereby minimizes the potential for error to be introduced by gradients in the refractive index of the air or other effects. In general, the lens should be selected to have the shortest focal length which is practical.

The lens must also be able to effectively transmit the light from the LED targets used by the system. These targets emit light with a wavelength of 860nm, in the near infra-red region of the spectrum. Lenses used for imaging this wavelength usually require a special coating to be applied to their optical surfaces, or at least the absence of the NIR blocking coatings which are used on most photographic lenses.

2.2.8 Camera Body and Mechanical Design

The body of the camera must maintain the position of the lens and sensor relative to one another and relative to the other cameras in the network. The body should therefore be stiff, and as immune to thermal deformation as possible. With these criteria in mind, the camera bodies were machined from solid blocks of Invar. The free machining version of the alloy was used as this was a requirement of the machine shop doing the fabrication. The Invar 36 alloy has a coefficient of thermal expansion (CTE) of approximately 1.5 ppm/˚C for temperatures between 20˚C and 100˚C [23]. Although the system is not expected to endure great fluctuations in temperature, it is helpful to understand the potential for temperature related expansion and contraction of mechanical components to introduce error into the measurements. We can see, in the figure below, that the expansion or contraction of the camera body moves the lens and sensor relative to one another. If the target image is at the center of the sensor this movement isn't seen in the image, but a target image at any other location on the sensor has its position on the sensor altered. The apparent position depends both on the movement of the sensor relative to the lens and the expansion of the sensor itself. The sensor, being made of silicon, is assumed to have a CTE of 2.5 ppm/˚C [24].

If the target is close to the edge of the sensor, the error is maximized. An estimate of the worst case error can be made. In image coordinates, the error is:

$$e = 1.5\frac{ppm}{^{\circ}C} * 18mm - 2.5\frac{ppm}{^{\circ}C} * 18mm = 18\frac{nm}{^{\circ}C}$$

This translates into an error of 720nm/˚C in the position of a target 1m away from the camera. The estimation assumes that the temperature of the sensor and the camera body will be the same. This is not necessarily true due to the localized generation of heat from the camera electronics. Since the magnitude of the error is quite small, further analysis or temperature compensation is not considered necessary. However, it is worth noting that the difference in CTE between silicon and steel (~10 ppm/˚C), or between silicon and aluminum (~20 ppm/˚C) would cause this error to be significant, on the order of the measurement precision of the system.

The image sensor is attached to the camera body through a thin aluminum mounting plate. The sensor's ceramic package is glued to the plate using epoxy, and the plate is then bolted to the camera body. This removes the relatively soft and unstable PCB from the measurement chain of the device. To avoid greatly over constraining the sensor, the PCB to which it is soldered (Sensor Board) is not rigidly attached to the camera body, but is left suspended by the image sensor pins and the pins of the connectors to the FPGA board.

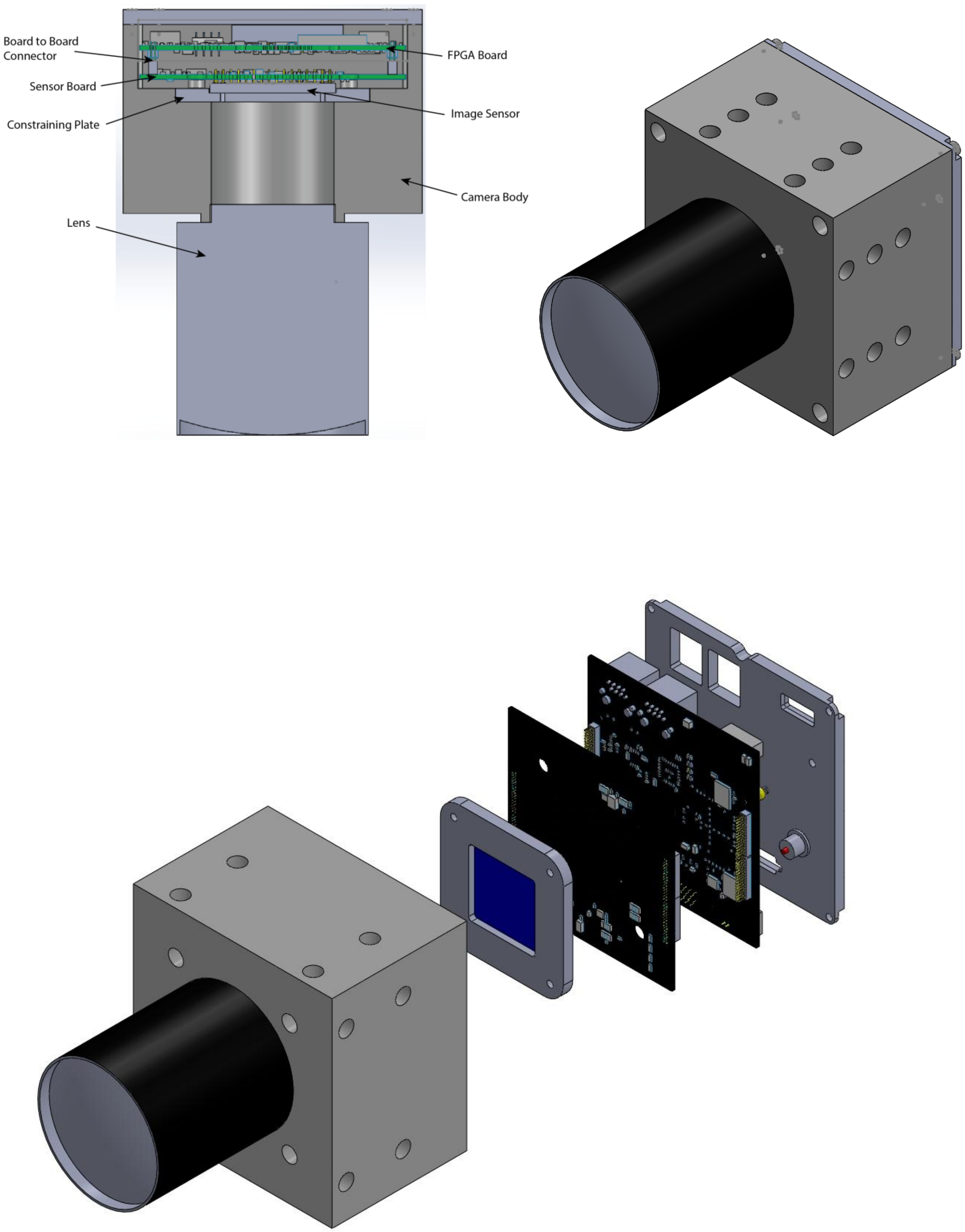

Figure 4: Camera CC (*top left*), Camera exterior (*top right*), Camera Exploded View (*bottom*)

2.3 Handheld Probe Design

The ideal way to measure feature locations with an optical system would be to measure them directly because this results in the shortest measurement chain, without the potential for error from deflection, poor construction, or poor calibration of the probe. This, however, is difficult because it requires the system to identify the features of interest in the scene, and in the case of a photogrammetric network to determine which features correspond to which between multiple images. Because of this, it is much more practical to insert a feature into the scene which can easily be distinguished from the background and identified by each camera. In order to do this, a probe is used which allows the target to be moved to different positions so that features of another object can be measured.

The simplest probe design is one that puts the target in direct contact with the feature to be measured. One could design such a probe by having a cat's eye reflector as the probing ball. There would then be very little opportunity for the probe to introduce error into the measurement by expanding, contracting, or flexing. The downside of this device is that it becomes impossible to probe any interior features since the target would be obscured from view. This makes such a probe impractical for use in most industrial situations. The next simplest probe design has two targets which are perfectly aligned with the probing tip. This design makes the calculation of the probe tip location simple, the two targets define a line and the probe tip is located at a known distance along that line [4]. The downside to this probe is that it must be very accurately constructed, since any misalignment between the three points will not be able to be compensated. Because of these difficulties, it is necessary to use a probe with three or more targets. The measurement of three targets fully defines the pose of an arbitrary body. This means that the probe does not need to be constructed with any pre-defined relationship between the targets and the probing tip. All that is needed is for their locations to remain constant on the probe body.

Since the probe does not need to maintain any special relationship between the tip and the targets, the criteria for its design are:

- To make the targets visible during probing
- To position the targets such that an accurate measurement of the probe pose can be obtained
- To minimize movement of the targets relative to the probing tip
- To be convenient to hold and move around the object to be measured

To make the targets visible during probing they must be positioned sufficiently far from the probing tip that they won't be obscured by features of the object being probed. In order for an accurate measurement of the probe pose to be obtained the targets can't be too close together. If the targets are too close together, small errors in the measurement of the target positions are transformed into large errors in the measurement of the probe orientation and therefore the probe tip position. A reasonable compromise is to place the targets approximately as far from each other as the centroid of the targets is from the probe tip. This keeps the error in the probe tip position measurement similar to the error in the target measurement. Once the locations of the targets are chosen, the focus of the probe design is on maintaining these positions.

2.3.1 Probe Mechanical Design

During use the probe will be subjected to some force from the operator. While the operator should try to minimize the force applied to the probe, it is necessary to have some force to ensure that the probe ball is in contact with the surface being measured. The design of the probe needs to minimize the movement of the targets relative to the probing tip under this force.

This is done by making the probe body very stiff. There will always be some movement in the operator's hand, at least on the scale that we are measuring, so the connection between the handle of the probe and the probe body should be comparatively flexible.

In order to keep the probe body light enough to be held easily, it is constructed from a piece of carbon fiber Nomex honeycomb panel. A bracket and epoxy are used to join a threaded insert to the bottom of the panel where a standard probe tip can be attached. This allows different probe tips to be used, however a calibration must be performed for each one.

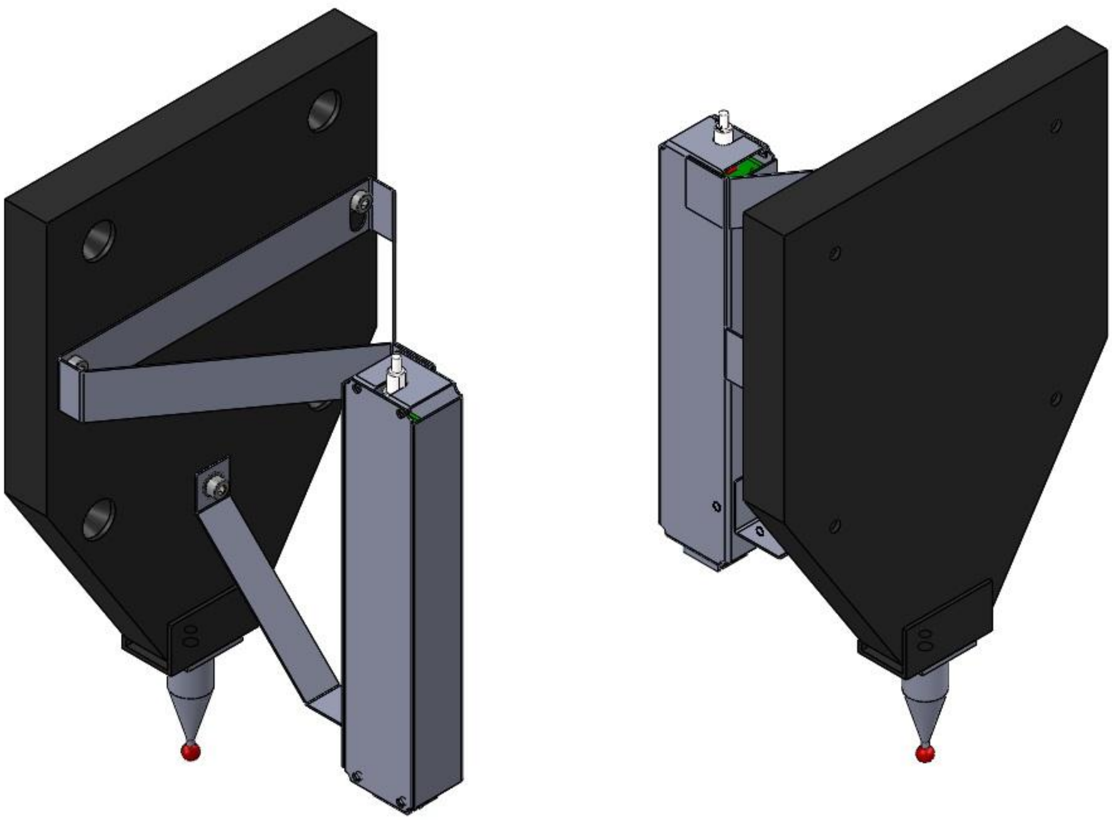

Figure 5: The Handheld Probe Design

This probe body design is very stiff. The analysis in Appendix B indicates that the probe is most flexible in bending, where its stiffness is approximately 25nm/N. Thermal expansion of the probe is a greater concern than bending. The analysis in Appendix A shows that the body will expand at a rate of 1.75 μm/˚C. This is still quite small when compared to the tracking accuracy of the cameras.

2.3.2 Probe Target Selection

Photogrammetric systems commonly use one of two broad types of optical targets: retro-reflectors or light emitters. Retro-reflector targets can be cat's eye reflectors (glass spheres), or flat pieces of retro-reflective tape. Light emitting targets can be any light source which produces consistent illumination. LEDs are commonly used.

Since the angle of the probe relative to the cameras is changing constantly, it is important for the targets to provide a consistent image regardless of orientation. This means that the retro-reflective tape targets are not suitable since they appear to have a different shape when viewed from different angles. It seems that the cat's eye retro-reflectors could be used, but they would need to be mounted outside of the probe body so that the whole sphere was visible to the camera in all measured orientations. LED targets can be mounted flush with the front surface of the probe and provide a point source of light which appears the same when viewed from a wide range of angles. Most LEDs do not provide a uniform intensity of light across different viewing angles. Since the camera will have a fixed exposure time during operation, it is best to have the light output from the target stay constant. As described by Rao [10] the HE8812SG LEDs provide such an illumination pattern, where the light intensity remains constant across a range of more than 90˚.

2.4 Real-Time Reconstruction Algorithm and Software Design

The reconstruction of the target positions and the probe ball tip position is done in the TwinCAT operating system in real-time. Two modules were designed in MATLAB/Simulink to perform the two functions. The TwinCAT target for MATLAB/Simulink (TE1400) was used to generate the target code which was used in the TwinCAT configuration.

2.4.1 Target Position Reconstruction Algorithm

The reconstruction of the target positions in world coordinates, using their positions in pixel coordinates is done in two steps. In the first step, the positions in pixel coordinates are corrected for distortion and transformed to image plane coordinates. The second step involves the triangulation of the target position in world coordinates using the image plane positions from multiple cameras. The distortion correction is done onboard the individual cameras. The distortion terms are calculated using the distorted image coordinates, instead of the undistorted coordinates, as the distortion magnitudes are small. First, the pixel coordinate positions are transformed into distorted positions in image coordinates:

$$x_d = \frac{1}{S_x}(u_i - u_0)$$

$$y_d = \frac{1}{S_y}(v_i - v_0)$$

The radial distortion is:

$$\delta x_{i,rad} \approx x_d(k_1({x_d}^2 + {y_d}^2) + k_2({x_d}^2 + {y_d}^2)^2)$$

$$\delta y_{i,rad} \approx y_d(k_1({x_d}^2 + {y_d}^2) + k_2({x_d}^2 + {y_d}^2)^2)$$

The tangential distortion is:

$$\delta x_{i,tan} \approx 2p_1 x_d y_d + p_2(3{x_d}^2 + {y_d}^2)$$

$$\delta y_{i,tan} \approx p_1({x_d}^2 + 3{y_d}^2) + 2p_2 x_d y_d$$

The position in corrected image coordinates is:

$$x_i = x_d - \delta x_{i,rad} - \delta x_{i,tan}$$

$$y_i = y_d - \delta y_{i,rad} - \delta y_{i,tan}$$

The real-time computer is then sent the corrected image coordinates from each camera:

$$(x_{i,1}, y_{i,1}), (x_{i,2}, y_{i,2}), etc.$$

Referring to the camera model described in section 1.2.3, the following equations were obtained for the corrected image coordinates as a function of the target position in world coordinates:

$$x_i = f\frac{R_{11}X_w + R_{12}Y_w + R_{13}Z_w + x_0}{R_{31}X_w + R_{32}Y_w + R_{33}Z_w + z_0}$$

$$y_i = f\frac{R_{21}X_w + R_{22}Y_w + R_{23}Z_w + y_0}{R_{31}X_w + R_{32}Y_w + R_{33}Z_w + z_0}$$

These equations can be rewritten in a form which lends itself to the construction of a matrix system of equations:

$$x_i = \frac{L_1X_w + L_2Y_w + L_3Z_w + L_4}{L_9X_w + L_{10}Y_w + L_{11}Z_w + 1}$$

$$y_i = \frac{L_5X_w + L_6Y_w + L_7Z_w + L_8}{L_9X_w + L_{10}Y_w + L_{11}Z_w + 1}$$

Where $L_1 = \frac{fR_{11}}{z_0}$, $L_2 = \frac{fR_{12}}{z_0}$, $L_3 = \frac{fR_{13}}{z_0}$, $L_4 = \frac{fx_0}{z_0}$, $L_5 = \frac{fR_{21}}{z_0}$, $L_6 = \frac{fR_{22}}{z_0}$, $L_7 = \frac{fR_{23}}{z_0}$, $L_8 = \frac{fy_0}{z_0}$, $L_9 = \frac{R_{31}}{z_0}$, $L_{10} = \frac{R_{32}}{z_0}$, $L_{11} = \frac{R_{33}}{z_0}$.

An over determined system of equations can be constructed using these equations from multiple cameras:

$$\begin{bmatrix} x_{i,1} - L_{4,1} \\ y_{i,1} - L_{8,1} \\ \vdots \\ x_{i,n} - L_{4,n} \\ y_{i,n} - L_{8,n} \end{bmatrix} = \begin{bmatrix} L_{1,1} - L_{9,1}x_{i,1} & L_{2,1} - L_{10,1}x_{i,1} & L_{3,1} - L_{11,1}x_{i,1} \\ L_{5,1} - L_{9,1}y_{i,1} & L_{6,1} - L_{10,1}y_{i,1} & L_{7,1} - L_{11,1}y_{i,1} \\ \vdots & \vdots & \vdots \\ L_{1,n} - L_{9,n}x_{i,n} & L_{2,n} - L_{10,n}x_{i,n} & L_{3,n} - L_{11,n}x_{i,n} \\ L_{5,n} - L_{9,n}y_{i,n} & L_{6,n} - L_{10,n}y_{i,n} & L_{7,n} - L_{11,n}y_{i,n} \end{bmatrix} \begin{bmatrix} X_w \\ Y_w \\ Z_w \end{bmatrix}$$

This system can be simplified as:

$$B = \boldsymbol{A}P$$

The pseudo-inverse operation (‘pinv’) in MATLAB is used to calculate the Moore-Penrose pseudo-inverse, $\boldsymbol{A}^{+}$, of $\boldsymbol{A}$. Then the least squares solution for the point P in world coordinates is:

$$P = \boldsymbol{A}^{+} B$$

It is noted that the columns of $\boldsymbol{A}$ will be linearly independent as long as the camera origins are not collinear with the target point. Since this is the case, the Moore-Penrose pseudo-inverse can be calculated as:

$$\boldsymbol{A}^{+} = (\boldsymbol{A}^{\boldsymbol{T}}\boldsymbol{A})^{-1}\boldsymbol{A}^{\boldsymbol{T}}$$

This may be useful if the reconstruction algorithm needs to be written for a platform where high-level functions, such as MATLAB’s ‘pinv’, are not available. In the case of this optical CMM, MATLAB functions are available since code for the TwinCAT OS can be generated from Simulink models using Beckhoff’s TE1400 target for MATLAB/Simulink.

2.4.2 Probe Tip Position Reconstruction Algorithm

The probe tip reconstruction is done using Gower and Dijksterhuis' Procrustes method [16], discussed in section 1.3.2. The module calculates a rotation and translation which best match the target positions in the calibrated probe geometry to the measured target positions. This same coordinate transformation is then applied to the probe tip position from the calibrated probe geometry to get the measured probe tip position. The calibrated probe geometry values are saved in the matrix $\boldsymbol{X}_r$:

$$\boldsymbol{X}_r = \begin{bmatrix} x_{r1} & y_{r1} & z_{r1} \\ x_{r2} & y_{r2} & z_{r2} \\ x_{r3} & y_{r3} & z_{r3} \\ x_{r4} & y_{r4} & z_{r4} \end{bmatrix}$$

The centroid of the four target points is at the origin of the probe coordinate system.

Every time a measurement is taken, the measured target positions in the world coordinate system are used to create the matrix $\boldsymbol{X}_m$:

$$\boldsymbol{X}_m = \begin{bmatrix} x_{m1} & y_{m1} & z_{m1} \\ x_{m2} & y_{m2} & z_{m2} \\ x_{m3} & y_{m3} & z_{m3} \\ x_{m4} & y_{m4} & z_{m4} \end{bmatrix}$$

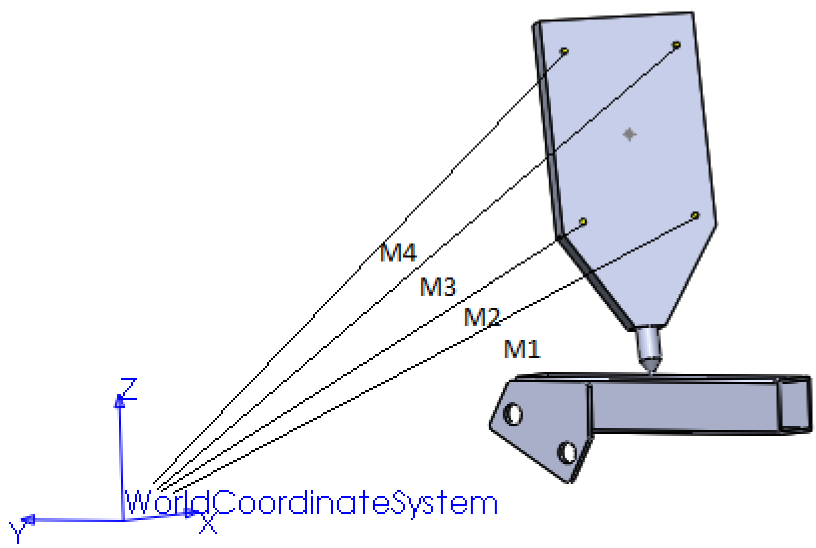

Figure 6: Measured target locations in the world coordinate system

An intermediate coordinate system is then defined which has the same orientation as the world coordinate system but has its origin located at the centroid of the four measured target locations.

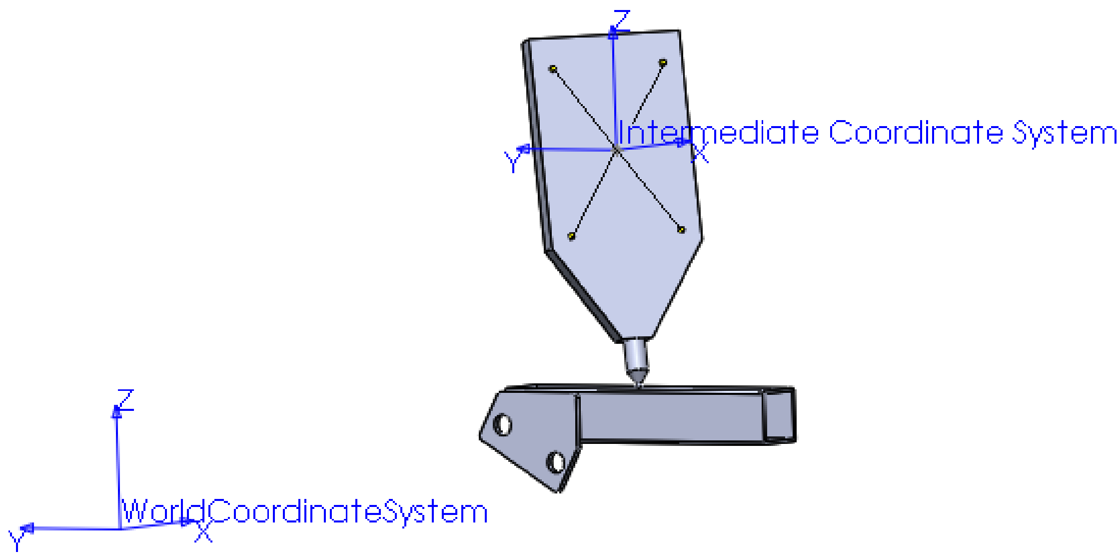

Figure 7: The target location vectors in the intermediate coordinate system

The target locations in the intermediate coordinate system are:

$$\boldsymbol{X}_{m,c} = \begin{bmatrix} x_{m1} & y_{m1} & z_{m1} \\ x_{m2} & y_{m2} & z_{m2} \\ x_{m3} & y_{m3} & z_{m3} \\ x_{m4} & y_{m4} & z_{m4} \end{bmatrix} - \begin{bmatrix} \frac{\Sigma x_{mi}}{4} & \frac{\Sigma y_{mi}}{4} & \frac{\Sigma z_{mi}}{4} \\ \frac{\Sigma x_{mi}}{4} & \frac{\Sigma y_{mi}}{4} & \frac{\Sigma z_{mi}}{4} \\ \frac{\Sigma x_{mi}}{4} & \frac{\Sigma y_{mi}}{4} & \frac{\Sigma z_{mi}}{4} \\ \frac{\Sigma x_{mi}}{4} & \frac{\Sigma y_{mi}}{4} & \frac{\Sigma z_{mi}}{4} \end{bmatrix}$$

The translation vector which relates the world coordinate system to the intermediate coordinate system is referred to as $\boldsymbol{T}$**:**

$$\boldsymbol{T} = \left[\frac{\Sigma x_{mi}}{4} \quad \frac{\Sigma y_{mi}}{4} \quad \frac{\Sigma z_{mi}}{4}\right]$$

The orthogonal procrustes problem is then solved to get the rotation matrix which best fits $\boldsymbol{X}_r$ to $\boldsymbol{X}_{m,c}$.

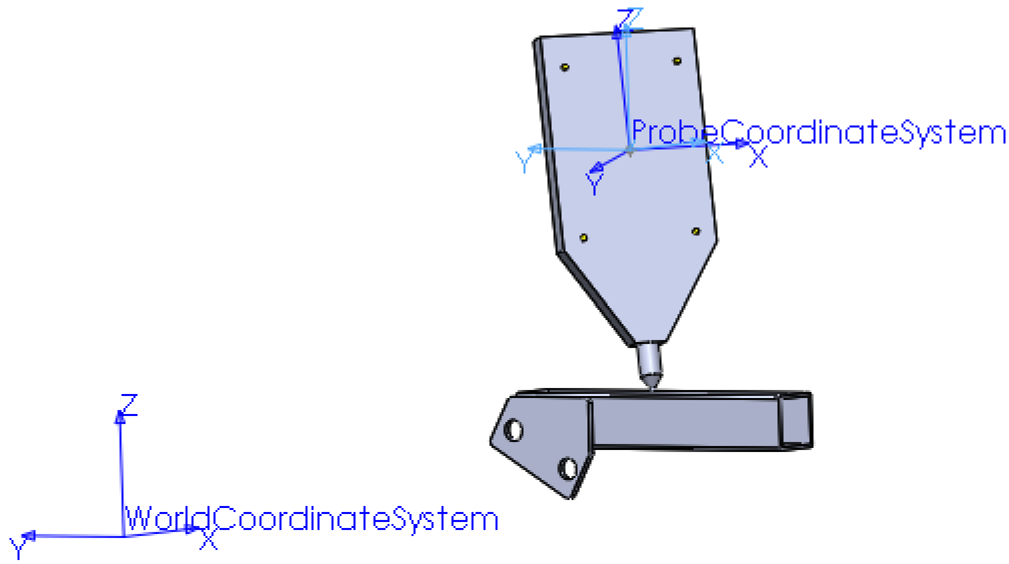

Figure 8: The probe coordinate system once it has been fit to the measured target locations

The singular value decomposition of $\boldsymbol{X_{m,c}}'\boldsymbol{X_r}$ is taken using the MATLAB function ‘svd’:

$$\boldsymbol{X_{m,c}}'\boldsymbol{X_r} = \boldsymbol{U\Sigma V}'$$

The rotation matrix $\boldsymbol{Q}$ is then given by:

$$\boldsymbol{Q} = \boldsymbol{VU}'$$

The rotation $\boldsymbol{Q}$ and the translation $\boldsymbol{T}$ are applied to the calibrated probe tip center location $\boldsymbol{P_r}$ to find its location in the world coordinate system:

$$\boldsymbol{P_m} = \boldsymbol{P_r Q} + \boldsymbol{T}$$

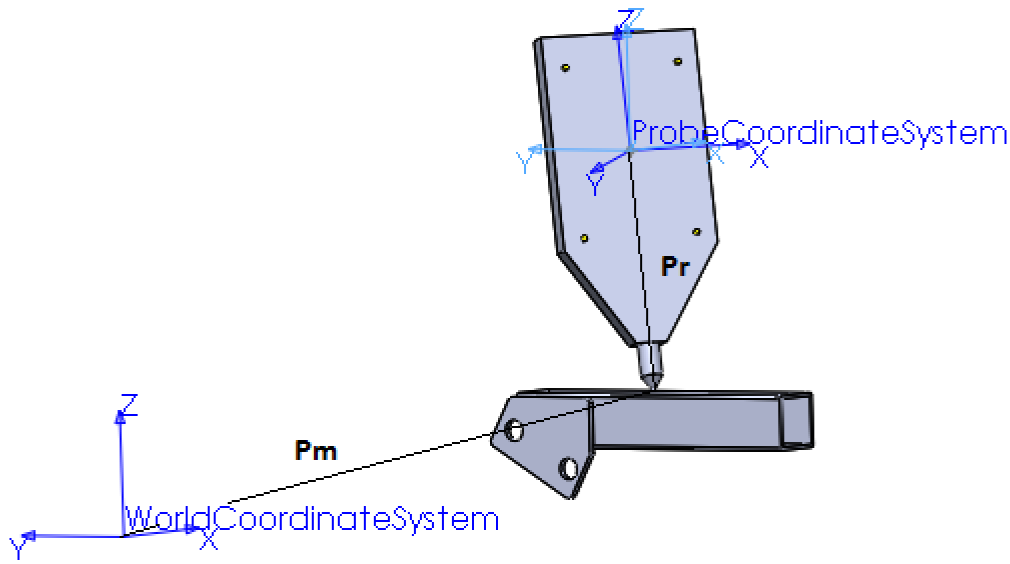

Figure 9:Probe tip measurement calculated from reference geometry

Chapter 3: Calibrating and Testing the Optical Dimension Measurement System

The system requires two calibration operations. The first calibration is required to find the unknown parameters in the target position reconstruction matrices. These are related to the position and orientation of the two cameras in the network, as well as the lens distortion. The second calibration is used to determine the geometry of the probe. This calibration relies on the camera system to measure the positions of the targets while the probe is rotated around the probe tip center.

3.1 Camera System Calibration

The camera system calibration requires a set of target images where the world coordinates of the targets are known, or at least some relationship between them is known. These reference points were generated by mounting an LED target to the probing head of a Mitutoyo Crysta-Apex CMM. The world coordinate measurements were taken from the CMM, while the target positions in camera coordinates were recorded from the camera system. The accuracy specification for the Crysta-Apex CMM is 1.7 µm+3 µm/m*L (where L is the length travelled), and its resolution is 0.1 µm.

The calibration volume was 400 mm x 400 mm x 15 mm and approximately 1 m away from the cameras. This allowed the results of the calibration to be compared with those of Rao [10] to ensure that the image sensor was performing well. To reduce the effect of random noise on the camera calibration, 100 measurements were averaged for every data point. The camera data and the CMM data were saved in a text file and the data processing was done in MATLAB. The calibration process used is the same as that described by Heikkila [9], and used by Rao [10] as a benchmark. The calibration is done in two stages, first a direct linear transformation is used to produce starting estimates of the parameters from the pinhole model, then a non-linear least squares optimization is done to fit these parameters along with the non-linear distortion parameters. Heikkila and Silven [9] use the following representation for the linear pinhole model used in the DLT:

$$\begin{bmatrix} u_i w_i \\ v_i w_i \\ w_i \end{bmatrix} = \begin{bmatrix} L_1 & L_2 & L_3 & L_4 \\ L_5 & L_6 & L_7 & L_8 \\ L_9 & L_{10} & L_{11} & L_{12} \end{bmatrix} \begin{bmatrix} X_i \\ Y_i \\ Z_i \\ 1 \end{bmatrix}$$

If L_{12} is set to 1 the following equations can be written for u_i and v_i:

$$u_i = L_1 X_i + L_2 Y_i + L_3 Z_i + L_4 - L_9 X_i u_i - L_{10} Y_i u_i - L_{11} Z_i u_i$$

$$v_i = L_5 X_i + L_6 Y_i + L_7 Z_i + L_8 - L_9 X_i v_i - L_{10} Y_i v_i - L_{11} Z_i v_i$$

To perform the DLT for one camera's parameters, the matrices $\boldsymbol{X}$ and $\boldsymbol{Y}$ can be constructed using the image coordinate system and world coordinate system target location values [9] [11].

$$\boldsymbol{X} = \begin{bmatrix} X_1 & Y_1 & Z_1 & 1 & 0 & 0 & 0 & 0 & -X_1 u_1 & -Y_1 u_1 & -Z_1 u_1 \\ 0 & 0 & 0 & 0 & X_1 & Y_1 & Z_1 & 1 & -X_1 v_1 & -Y_1 v_1 & -Z_1 v_1 \\ \vdots & \vdots & \vdots & \vdots & \vdots & \vdots & \vdots & \vdots & & \vdots\ \vdots\ \vdots & \\ X_N & Y_N & Z_N & 1 & 0 & 0 & 0 & 0 & -X_N u_N & -Y_N u_N & -Z_N u_N \\ 0 & 0 & 0 & 0 & X_N & Y_N & Z_N & 1 & -X_N v_N & -Y_N v_N & -Z_N v_N \end{bmatrix}$$

$$\boldsymbol{Y} = \begin{bmatrix} u_1 \\ v_1 \\ \vdots \\ u_N \\ v_N \end{bmatrix}$$

These can be used to express the system of equations relating the control points as:

$$\boldsymbol{XL} = \boldsymbol{Y}$$

Where $\boldsymbol{L}$ is the vector of unknown parameters:

$$\boldsymbol{L} = \begin{bmatrix} L_1 \\ L_2 \\ L_3 \\ L_4 \\ L_5 \\ L_6 \\ L_7 \\ L_8 \\ L_9 \\ L_{10} \\ L_{11} \end{bmatrix}$$

The least squares solution of the system of equations can be found by:

$$\boldsymbol{L} = (\boldsymbol{X^T X})^{-1} \boldsymbol{X^T Y}$$

Where $(\boldsymbol{X^T X})^{-1} \boldsymbol{X^T}$ is the Moore-Penrose pseudo-inverse of $\boldsymbol{X}$, whose columns are linearly independent.

This operation can be performed using the matrix left divide operation in MATLAB:

$$\boldsymbol{L} = (\boldsymbol{X^T X}) \backslash \boldsymbol{X^T Y}$$

Or equivalently, the left divide operation can solve the original system in a least squares sense directly:

$$\boldsymbol{L} = \boldsymbol{X} \backslash \boldsymbol{Y}$$

The linear parameters of the camera model can be extracted from the values of $\boldsymbol{L}$ [11]**:**

$$\boldsymbol{T} = \begin{bmatrix} L_1 & L_2 & L_3 \\ L_5 & L_6 & L_7 \\ L_9 & L_{10} & L_{11} \end{bmatrix}^{-1} \begin{bmatrix} -L_4 \\ -L_8 \\ -1 \end{bmatrix}$$

$$D = \pm \frac{1}{\sqrt{{L_9}^2 + {L_{10}}^2 + {L_{11}}^2}}$$

$$u_0 = D^2 (L_1 L_9 + L_2 L_{10} + L_3 L_{11})$$

$$v_0 = D^2 (L_5 L_9 + L_6 L_{10} + L_7 L_{11})$$

$$f_x = \sqrt{D^2((u_0L_9 - L_1)^2 + (u_0L_{10} - L_2)^2 + (u_0L_{11} - L_3)^2)}$$

$$f_y = \sqrt{D^2((v_0L_9 - L_5)^2 + (v_0L_{10} - L_6)^2 + (v_0L_{11} - L_7)^2)}$$

$$\boldsymbol{R} = D\begin{bmatrix} \frac{u_0L_9 - L_1}{f_x} & \frac{u_0L_{10} - L_2}{f_x} & \frac{u_0L_{11} - L_3}{f_x} \\ \frac{v_0L_9 - L_5}{f_x} & \frac{v_0L_{10} - L_6}{f_x} & \frac{v_0L_{11} - L_7}{f_x} \\ L_9 & L_{10} & L_{11} \end{bmatrix}$$

The sign of D is set so that the determinant of $\boldsymbol{R}$ is positive.

These parameters, determined from the DLT are then used as the starting point for the non-linear estimation of the parameters for the full camera model, including lens distortion. The initial estimates for the lens distortion parameters are 0.

Using 200 points for the calibration, and 200 points for evaluation, the RMS 3D error of the calibration is 23.6µm. This can be compared to an RMS 3D error of 18.2µm as reported by Rao [10] for calibration with the same number of points distributed in a similar fashion. This indicates that the camera is working reasonably well. The errors in the three world coordinate dimensions are listed in Table 1.

Table 1: Accuracy of the calibrated camera system at a range of 1m

3D (µm)	X-axis (µm)	Y-axis (µm)	Z-axis (µm)
23.6	4.6	22.7	4.6

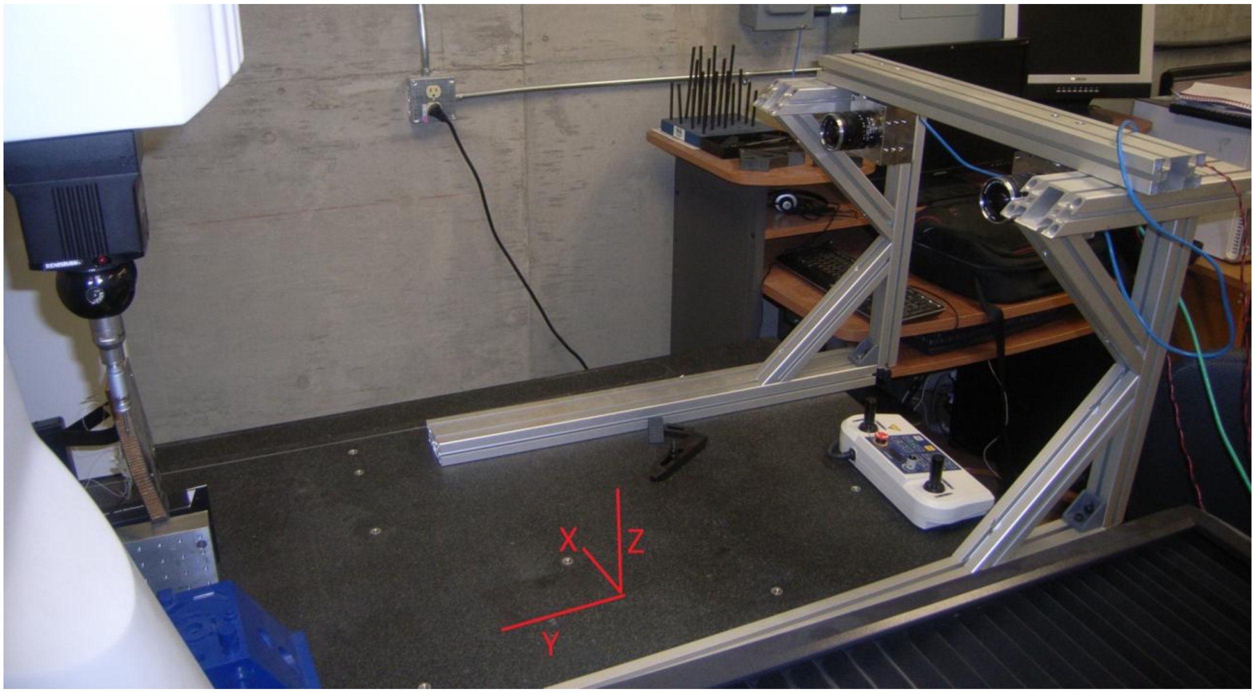

Figure 10: Photo of the Cameras on the CMM for calibration with axes labeled

To generate the best possible calibration using the data collected, the calibration is repeated with all 400 points. Since all the points are used in calibration, an error figure is not produced for this calibration so the system performance is assumed to be that shown in Table 1.

3.2 Probe Calibration

The probe calibration is done using the camera system to track the LED targets, and a reference block to position the probe tip in a stable location. The probe body is then rotated about its tip and the trajectories of the LED targets are recorded. By fitting spheres to the trajectories of the targets, the location of the probe tip center in the world coordinate system can be determined. Once this is known, the rigid body relationship between the LEDs and the probe tip can be determined by fitting a shape to their trajectories.

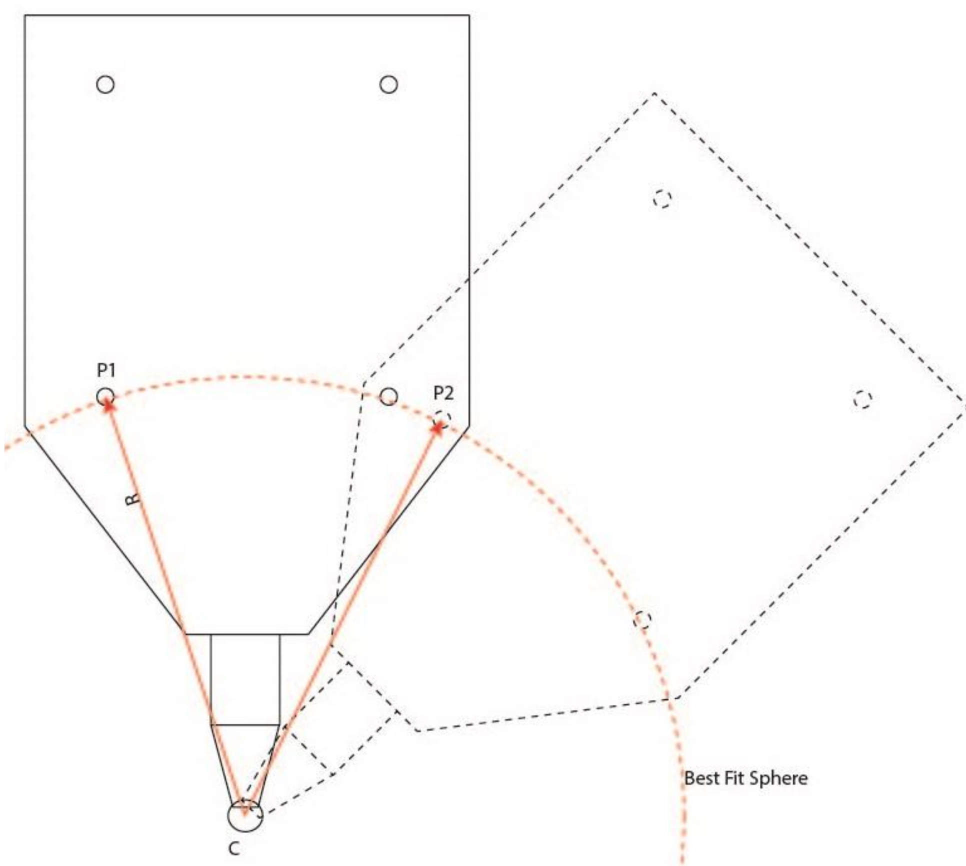

Figure 11: Fitting a sphere to target positions. P1 and P2 are the location of one LED at two different probe orientations

To find the probe center, the position coordinates for each of the four targets are recorded in four matrices in MATLAB:

$$\boldsymbol{T1} = \begin{bmatrix} x_{T1,1} & y_{T1,1} & z_{T1,1} \\ \vdots & \vdots & \vdots \\ x_{T1,n} & y_{T1,n} & z_{T1,n} \end{bmatrix}$$

$$\boldsymbol{T2} = \begin{bmatrix} x_{T2,1} & y_{T2,1} & z_{T2,1} \\ \vdots & \vdots & \vdots \\ x_{T2,n} & y_{T2,n} & z_{T2,n} \end{bmatrix}$$

$$\boldsymbol{T3} = \begin{bmatrix} x_{T3,1} & y_{T3,1} & z_{T3,1} \\ \vdots & \vdots & \vdots \\ x_{T3,n} & y_{T3,n} & z_{T3,n} \end{bmatrix}$$

$$\boldsymbol{T4} = \begin{bmatrix} x_{T4,1} & y_{T4,1} & z_{T4,1} \\ \vdots & \vdots & \vdots \\ x_{T4,n} & y_{T4,n} & z_{T4,n} \end{bmatrix}$$

Where n is the number of measurements.

For each of these matrices of target positions, a sphere is fit using the method described in section 1.3.1.2. In this notation $T1_{i,1}$corresponds to the x position of target 1 in the i^{th} measurement. The matrices representing the system of equations are then:

$$\boldsymbol{A}_{T1} = \begin{bmatrix} 2\sum_{i=1}^{n} T1_{i,1} & 2\sum_{i=1}^{n} T1_{i,2} & 2\sum_{i=1}^{n} T1_{i,3} & n \\ 2\sum_{i=1}^{n} {T1_{i,1}}^2 & 2\sum_{i=1}^{n} T1_{i,2}T1_{i,1} & 2\sum_{i=1}^{n} T1_{i,3}T1_{i,1} & \sum_{i=1}^{n} T1_{i,1} \\ 2\sum_{i=1}^{n} T1_{i,1}T1_{i,2} & 2\sum_{i=1}^{n} {T1_{i,2}}^2 & 2\sum_{i=1}^{n} T1_{i,3}T1_{i,2} & \sum_{i=1}^{n} T1_{i,2} \\ 2\sum_{i=1}^{n} T1_{i,1}T1_{i,3} & 2\sum_{i=1}^{n} T1_{i,2}T1_{i,3} & 2\sum_{i=1}^{n} {T1_{i,3}}^2 & \sum_{i=1}^{n} T1_{i,3} \end{bmatrix}$$

$$\boldsymbol{b}_{T1} = \begin{bmatrix} \sum_{i=1}^{n} {T1_{i,1}}^2 + \sum_{i=1}^{n} {T1_{i,2}}^2 + \sum_{i=1}^{n} {T1_{i,3}}^2 \\ \sum_{i=1}^{n} {T1_{i,1}}^3 + \sum_{i=1}^{n} {T1_{i,2}}^2 T1_{i,1} + \sum_{i=1}^{n} {T1_{i,3}}^2 T1_{i,1} \\ \sum_{i=1}^{n} {T1_{i,1}}^2 T1_{i,3} + \sum_{i=1}^{n} {T1_{i,2}}^3 + \sum_{i=1}^{n} {T1_{i,3}}^2 T1_{i,2} \\ \sum_{i=1}^{n} {T1_{i,1}}^2 T1_{i,3} + \sum_{i=1}^{n} {T1_{i,2}}^2 T1_{i,3} + \sum_{i=1}^{n} {T1_{i,3}}^3 \end{bmatrix}$$

$$\boldsymbol{x}_{T1} = \begin{bmatrix} a_{T1} \\ b_{T1} \\ c_{T1} \\ {r_{T1}}^2 - {a_{T1}}^2 - {b_{T1}}^2 - {c_{T1}}^2 \end{bmatrix}$$

The system of equations is:

$$\boldsymbol{A}_{T1}\boldsymbol{x}_{T1} = \boldsymbol{b}_{T1}$$

The solution for $\boldsymbol{x}_{T1}$is:

$$\boldsymbol{x}_{T1} = \boldsymbol{A}_{T1}{}^{-1}\boldsymbol{b}_{T1}$$

In MATLAB, this can be solved using the matrix left division operator:

$$\boldsymbol{x}_{T1} = \boldsymbol{A}_{T1}\backslash\boldsymbol{b}_{T1}$$

Since a sphere can be fit to the trajectory of each of the four targets, four measurements are made of the target center location. The average of these four locations is used as the final calibrated value.

$$\begin{bmatrix} x_{cal} \\ y_{cal} \\ z_{cal} \end{bmatrix} = \begin{bmatrix} a_{T1} \\ b_{T1} \\ c_{T1} \end{bmatrix}/4 + \begin{bmatrix} a_{T2} \\ b_{T2} \\ c_{T2} \end{bmatrix}/4 + \begin{bmatrix} a_{T3} \\ b_{T3} \\ c_{T3} \end{bmatrix}/4 + \begin{bmatrix} a_{T4} \\ b_{T4} \\ c_{T4} \end{bmatrix}/4$$

Now that the probe tip center location is known, it is possible to use one set of measured target positions as the calibrated geometry. However, the effect of random and systematic noise on the calibrated geometry can be reduced by taking an average of all of the measurements. Since the measurements were all taken with the probe in different positions, a Procrustes method is used to align them all with each other. To do this, Gower & Dijksterhuis' group average algorithm, discussed in section 1.3.2 is used. Each target position has the calibrated position of the tip center subtracted, so that the rotation used in the Procrustes fit happens around the tip center position. The subtracted target position sets are contained in matrices, such that:

$$\boldsymbol{X_j} = \begin{bmatrix} x_{T1,j} - x_{cal} & y_{T1,j} - y_{cal} & z_{T1,j} - z_{cal} \\ x_{T2,j} - x_{cal} & y_{T2,j} - y_{cal} & z_{T2,j} - z_{cal} \\ x_{T3,j} - x_{cal} & y_{T3,j} - y_{cal} & z_{T3,j} - z_{cal} \\ x_{T4,j} - x_{cal} & y_{T4,j} - y_{cal} & z_{T4,j} - z_{cal} \end{bmatrix}$$

$\boldsymbol{X_1}$is used as the starting estimate for the group average $\boldsymbol{G}$:

$$\boldsymbol{G} = \boldsymbol{X_1}$$

Transformation $\boldsymbol{Q_j}$ is the orthogonal 3X3 matrix that best satisfies the equation: $\boldsymbol{G} = \boldsymbol{X_j}\boldsymbol{Q_j}$.

Using the Procrustes method described in section 1.3.2, the singular value decomposition of the product of $\boldsymbol{G'X_j}$ is taken:

$$\boldsymbol{G'X_j} = \boldsymbol{U_j}\boldsymbol{\Sigma}_{\mathbf{j}}\boldsymbol{V_j}'$$

The transformation is given by:

$$\boldsymbol{Q_j} = \boldsymbol{V_j}\boldsymbol{U_j}'$$

And the residual sum of squares is:

$$s_j = \|\boldsymbol{G}\| + \|\boldsymbol{X_j}\| + 2 * trace(\boldsymbol{\Sigma}_{\mathbf{j}})$$

Once the transformations are calculated for every set of points, the group average can be updated:

$$\boldsymbol{G} = \frac{1}{K}\sum_{j=1}^{K}\boldsymbol{X_j}\boldsymbol{Q_j}$$

The group residual is the sum of all of the residual sums of squares for each data set relative to the group average:

$$S = \sum_{j=1}^{K} s_j$$

The magnitude of the residual is used to determine whether the algorithm has converged. When the residual is no longer reduced significantly between iterations the algorithm is stopped, and the group average $\boldsymbol{G}$ is taken as the calibrated geometry.

3.2.1 Simulation of Probe Calibration Accuracy

Since it is not practical to measure the probe dimensions directly to verify the accuracy of the probe calibration, a simulation was done in MATLAB to quantify the amount of error which is likely to occur in the probe calibration process. First, a probe geometry was chosen, whose dimensions are approximately equal to those of the actual probe. The positions of the four targets relative to the probe tip center are given in Table 2.

Table 2: Probe LED locations for simulation of probe calibration accuracy

Target	X (mm)	Y (mm)	Z (mm)
1	-50	0	118
2	-50	0	228
3	50	0	118
4	50	0	228

$$\boldsymbol{t1}_0 = \begin{bmatrix} -50 \\ 0 \\ 118 \end{bmatrix}$$

$$\boldsymbol{t2}_0 = \begin{bmatrix} -50 \\ 0 \\ 228 \end{bmatrix}$$

$$\boldsymbol{t3}_0 = \begin{bmatrix} 50 \\ 0 \\ 118 \end{bmatrix}$$

$$\boldsymbol{t4}_0 = \begin{bmatrix} 50 \\ 0 \\ 228 \end{bmatrix}$$

This geometry is shown in Figure 12.

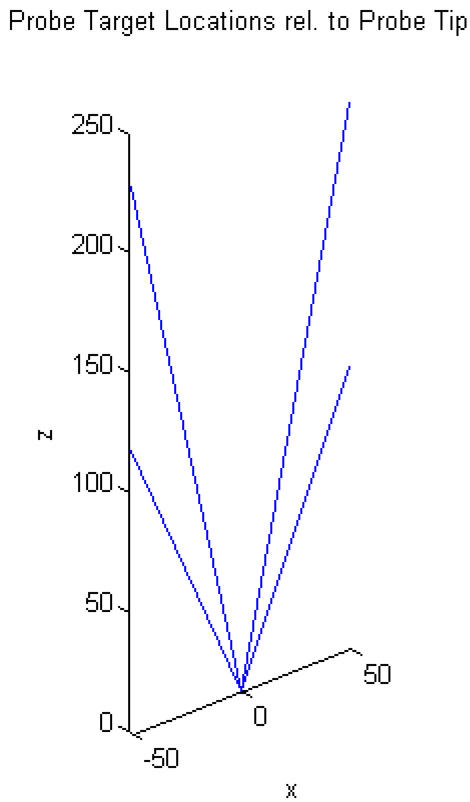

Figure 12: Probe geometry for simulation of probe calibration accuracy

In order to generate test points, a series of 10000 trios of angles were generated, with each being restricted to a certain range. These ranges were estimated to correspond to the practical limits of rotation when the probe is held in the hole of the block, they are listed in Table 3. The MATLAB function 'randn' was used to generate angles in the range, which were put in a matrix.

Table 3: Ranges of rotation angles used for simulation of probe calibration accuracy

$\alpha\ range\ (rad)$	$\beta\ range\ (rad)$	$\gamma\ range\ (rad)$
$\pm\pi/4$	$\pm\pi/4$	$\pm\pi/18$

$$Angle = \begin{bmatrix} \alpha_1 & \beta_1 & \gamma_1 \\ \vdots & \vdots & \vdots \\ \alpha_{10000} & \beta_{10000} & \gamma_{10000} \end{bmatrix}$$

These were then used to rotate the probe geometry. Rotation matrices were created from the values in the Angle matrix and applied to the upright probe target positions.

$$\boldsymbol{Rz_n} = \begin{bmatrix} cos(\gamma_n) & -sin(\gamma_n) & 0 \\ \sin(\gamma_n) & cos(\gamma_n) & 0 \\ 0 & 0 & 1 \end{bmatrix}$$

$$\boldsymbol{Ry_n} = \begin{bmatrix} \cos(\beta_n) & 0 & sin(\beta_n) \\ 0 & 1 & 0 \\ -sin(\beta_n) & 0 & cos(\beta_n) \end{bmatrix}$$

$$\boldsymbol{Rx_n} = \begin{bmatrix} 1 & 0 & 0 \\ 0 & cos(\alpha_n) & -sin(\alpha_n) \\ 0 & sin(\alpha_n) & cos(\alpha_n) \end{bmatrix}$$

$$\boldsymbol{t1}_n = \boldsymbol{Rz_n Ry_n Rx_n t1}_0$$

The error introduced by the camera was simulated by adding random, normally distributed, noise in X, Y, and Z axes to the data points. The standard deviation of the noise in each axis was set to the RMS positioning error of the camera system in that axis (4.6µ, 22.7µ, and 4.6µ, respectively). A set of points generated for one simulation run is shown in Figure 13.

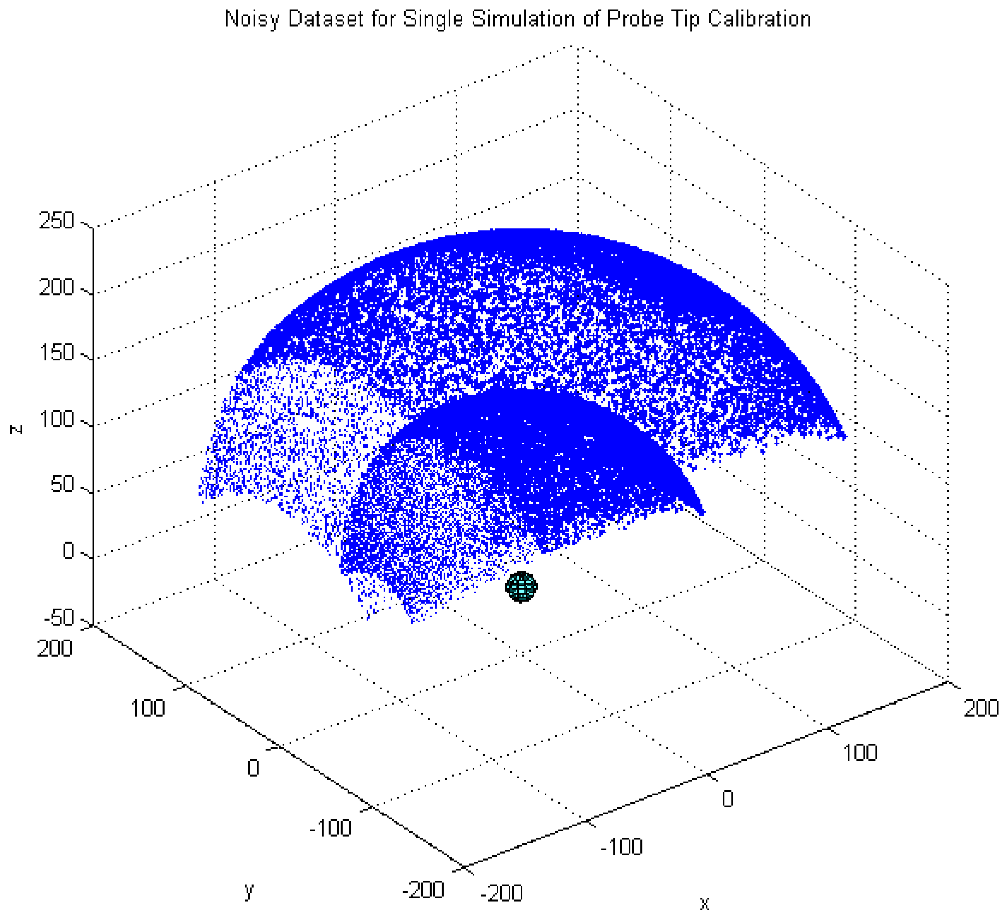

Figure 13: 3D plot of a dataset used for simulation of probe calibration accuracy

Spheres were then fit to these LED trajectories, using the method described in section 1.3.1. The 'calibrated' probe tip location was taken to be the average of the centers of these spheres. This process was repeated 3000 times to get a measure of the typical error present. The rms value of the probe tip location error was 0.42µm, while the error in all cases was less than 1.5µm. A histogram of the error in all 3000 simulation runs is shown in Figure 14.

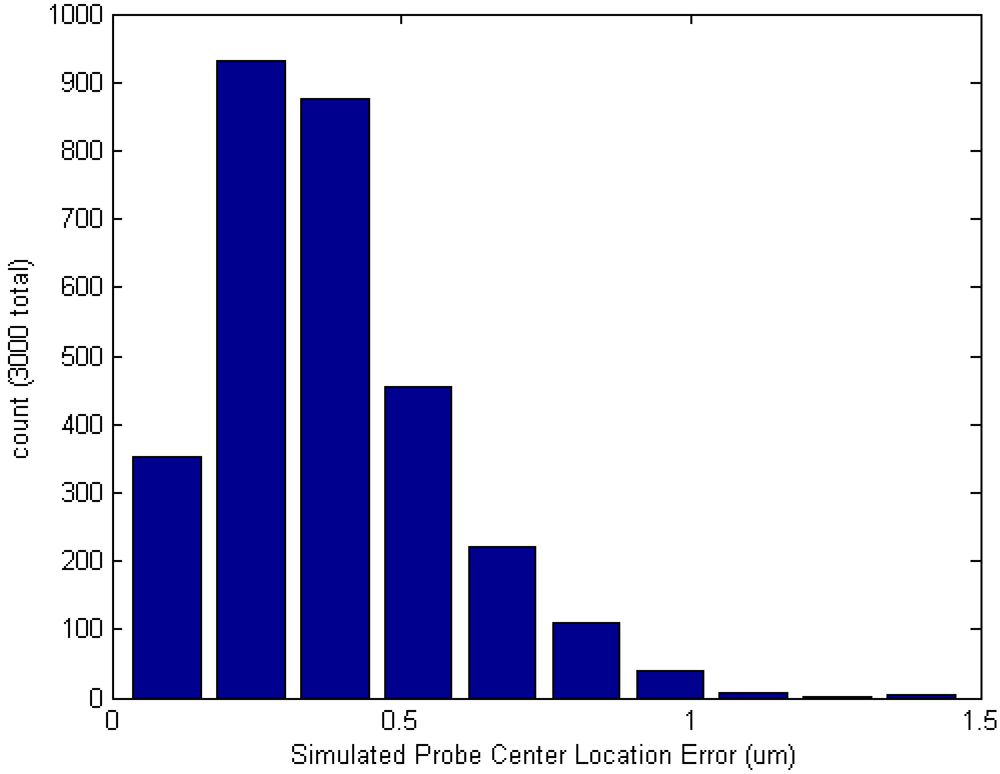

Figure 14: Histogram of probe center location error for 3000 simulation runs

Once the probe tip center location is found, the probe target locations are calibrated. The error in probe target location calibration is estimated by comparing the calibrated geometry to the known probe geometry. The calibrated geometry $\boldsymbol{G}$ is transformed to align with the starting geometry $\boldsymbol{X_0}$:

$$\boldsymbol{X_0}'\boldsymbol{G} = \boldsymbol{U_{test}}\boldsymbol{\Sigma}_{\mathbf{test}}\boldsymbol{V_{test}}'$$

$$\boldsymbol{Q_{test}} = \boldsymbol{V_{test}}\boldsymbol{U_{test}}'$$

$$\boldsymbol{G_{aligned}} = \boldsymbol{G}\boldsymbol{Q_{test}}$$

The difference between the initial and calibrated points is then taken:

$$\boldsymbol{Err} = \boldsymbol{G_{aligned}} - \boldsymbol{X_0}$$

Each row of the $\boldsymbol{Err}$ matrix represents the error in one target's calibrated position. To quantify the accuracy of the calibration, the average of the errors for each target position is taken for each simulation:

$$error = \frac{\|\boldsymbol{Err}(\mathbf{1},:)\| + \|\boldsymbol{Err}(\mathbf{2},:)\| + \|\boldsymbol{Err}(\mathbf{3},:)\| + \|\boldsymbol{Err}(\mathbf{4},:)\|}{4}$$

Where $\|\boldsymbol{Err}(\mathbf{1},:)\|$ is the magnitude of the first row of the matrix $\boldsymbol{Err}$. The histogram of this error value for all 3000 simulation runs is shown in Figure 15.

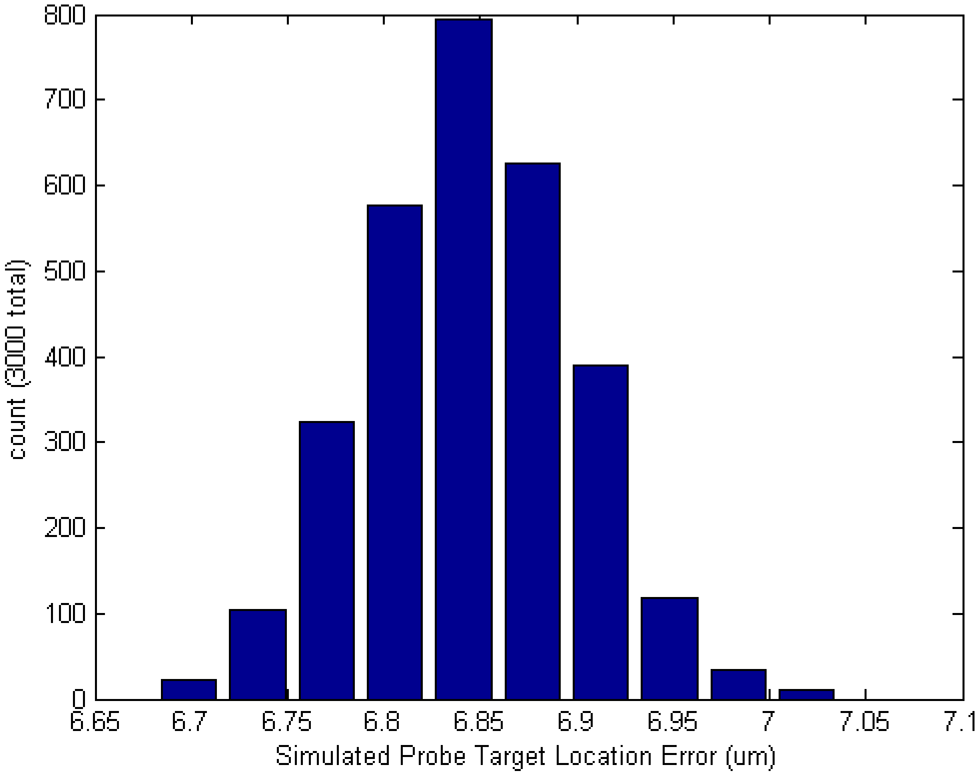

Figure 15: Histogram of the average target location error for all simulation runs

3.2.2 Probe Calibration Results

The data for the probe calibration was collected with the probe tip resting in the hole of a test piece bolted to the platform of the Mitutoyo CMM. 9673 measurements were taken while the probe was rotated by hand about the stationary probe tip. The data is plotted in Figure 16. Due to the shape of the probe and the test piece, it was difficult to sweep the probe through the range of angles used in the simulation while keeping the probe ball resting in the hole. Because of this, the calibration data does not cover as large a range of angles as was estimated in the simulation.

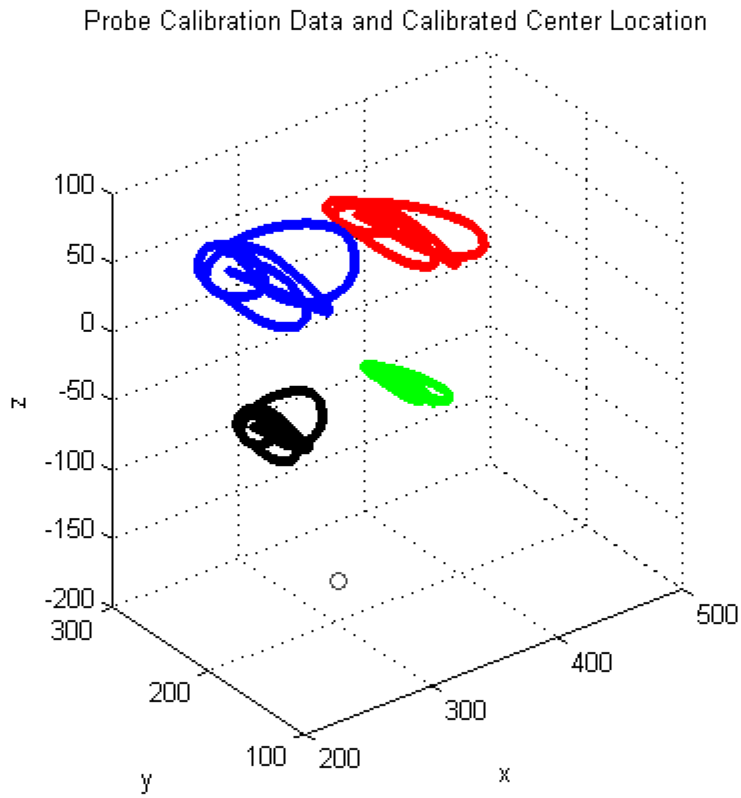

Figure 16: Calibration data and calibrated center location

Comparing the locations of the centers of the four fitted spheres gives an indication of the accuracy of the probe calibration in practice. The locations of the centers of the four spheres relative to the calibrated probe tip location are shown in Table 4. The residual error in the center location from sphere fitting is 5.2 µm. This is an order of magnitude higher than what was predicted by the simulation where the average was ~0.5 µm. This may be due to the smaller angular range of the calibration data set. It could also indicate that the error in the camera system has a systematic component which is not taken into account by the simulation. While the error is greater than expected, it is of comparable magnitude to the error in camera calibration and is therefore considered acceptable since it will not significantly degrade the performance of the system overall.

Table 4: Deviation in sphere center locations from probe calibration

Target	X (µm)	Y (µm)	Z(µm)	Distance (µm)
1	-0.64022	-2.2636	-0.71076	2.457427
2	0.232291	-1.19088	-0.76173	1.432619
3	1.455569	-4.82995	2.181227	5.495898
4	-1.04764	8.284439	-0.70874	8.380442

3.3 Overall System Testing Results

In order to test the system performance, two simple probing tests were performed. For these tests, the probe was held by hand and the system operated as it would be in a typical part checking scenario.

3.3.1 Thickness and Coplanar Measurement Test

In this test, the probe was used to measure the thickness of a rectangular block. The block is a steel piece of clamping hardware for the Mitutoyo CMM made of two stepped pieces which fit together. The thickness of the block was measured with a pair of digital calipers to be 20.34mm. The block was then clamped to the surface of the Mitutoyo CMM bed and the probe was used to measure a number of points on the CMM bed and on the top surface of the block. Two sets of measurements were recorded. The probe was set aside and a few minutes elapsed between the two tests, but the block was not unclamped or moved.

The data was analyzed in MATLAB. First a plane was fit to the points which were measured on the CMM bed surface. Then the distance between the plane and each of the points measured on the block surface was calculated. The thickness of the block was taken to be the average of these distances. The points and the best fit planes for both tests are shown in Figure 17 and Figure 18 on the next page.

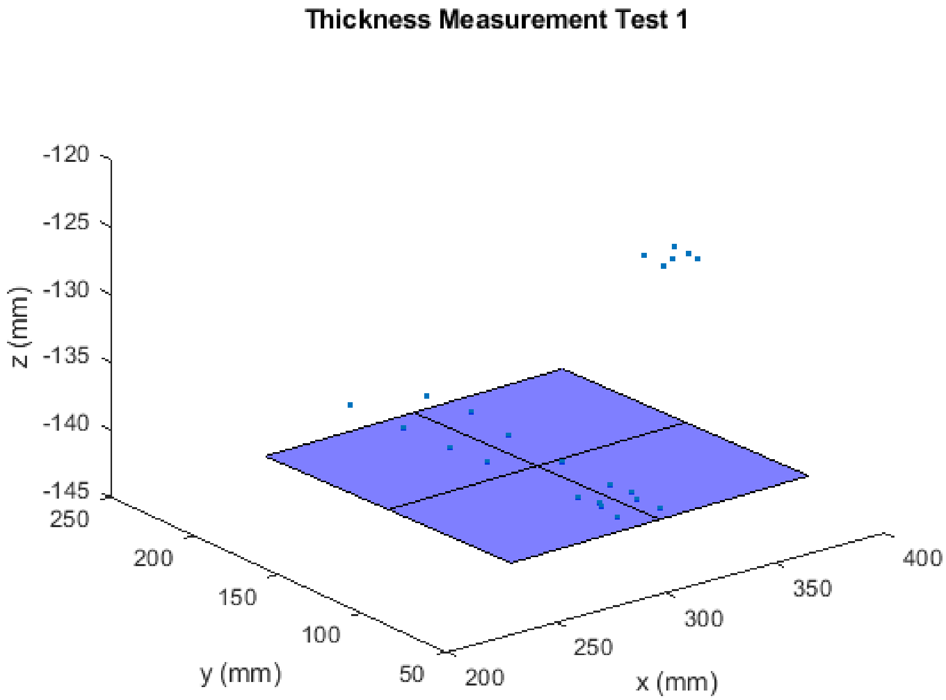

Figure 17: Plot of probed points for the first thickness test

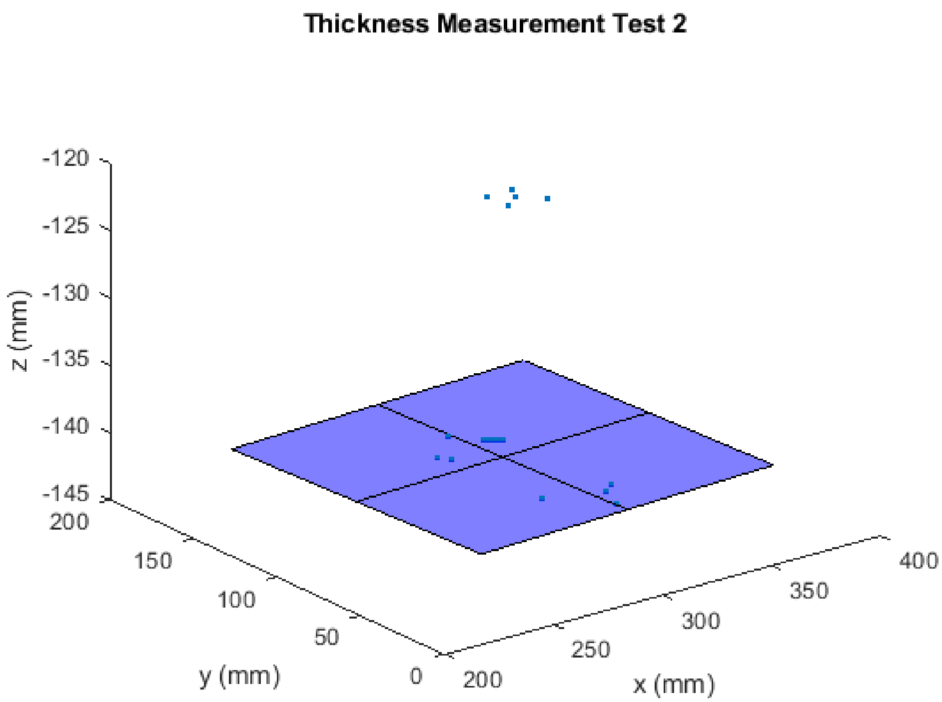

Figure 18: Plot of probed points for the second thickness test

This test shows the performance of the system in two ways; the deviation of the coplanar points from the best fit plane, and the deviation of the measured block thickness from the caliper measurement.

Table 5: Results of Coplanarity and Thickness Tests

Test 1				Test 2			
Bottom Surface		Top Surface		Bottom Surface		Top Surface	
Distance(mm)	rms (mm)	Distance (mm)	Average (mm)	Distance(mm)	rms (mm)	Distance (mm)	Average (mm)
-0.003313494	0.0041	20.3249348	20.332	-0.001528752	0.0025	20.33306045	20.33593138
0.00307882		20.33074578		0.002722933		20.32768725	
-0.009132609		20.35160148		0.00289448		20.35223176	
-0.00178629		20.32824571		0.000989466		20.34124762	
-0.002161067		20.32307896		0.001651201		20.31175982	
-0.002262867		20.33519012		0.000942097		20.34960135	
0.006494605				-0.004924108			
0.00884983				0.00198845			
0.002778355				0.001117496			
-0.00143765				-0.001217211			
0.000130388				0.001471188			
-0.002616811				-0.002512393			
0.00224078				0.001374795			
0.002679108				-0.002901807			
-0.001176928				-0.000318727			
-0.002364169				-0.004908481			
				0.003159374			

These deviation data are shown in Table 5. In both tests the coplanarity of the data is very good, the rms deviations from the two planes are 4.1 µm and 2.5 µm respectively. The thickness measurement is also very good, both measurements agree with the caliper measurement within 7 µm. While this result is very good, it is important to note that this test is not very sensitive to error in the Y-axis of the system. As noted in Camera System Calibration (p.41), the Y-axis has higher measurement error than the X- and Z-axes.

3.3.2 Calibration Ball Measurement Test

For this test a reference sphere artifact was probed. This sphere is a calibration ball produced by Mitutoyo for calibration and testing of their CMMs and is very accurate. The sphere is supplied with a calibration sheet which indicates that its' diameter is 19.989mm. The measurements were recorded using PolyWorks with the data streaming through the plug-in program developed as part of this project. The sphere was measured once beforehand to calibrate the probe tip diameter. In order to measure the sphere, it was screwed into the table of the CMM to which the optical CMM cameras were also attached. The distance between the cameras and the sphere was approximately 1m. During measurement the probe was positioned near, but not inside the calibration volume of the camera system. The sphere was measured three times. The measured position and diameter are shown in Table 6.

Table 6: Measurement results for the Mitutoyo CMM calibration ball

			Center Position (mm)				
Measurement	# Points	Diameter (mm)	X	Y	Z	Std. Dev. (mm)	RMS Error (mm)
1	8	19.907	249.894	60.891	-154.072	0.013	0.012
2	8	19.912	249.903	60.872	-154.087	0.018	0.017
3	8	19.894	249.892	60.863	-154.08	0.009	0.009

Table 7: Center location repeatability for spherical test artifact

Measurements	Center-Center Dist (mm)
1,2	0.025826343
2,3	0.01584298
1,3	0.029189039

The repeatability of the diameter measurement was 18µm, and the repeatability of the center location measurement was 30 µm. The fitting error for the spheres was less than 18 µm in all three cases. There is a somewhat larger discrepancy, of ~80µm, between the measured sphere diameters and the calibration certificate for the sphere. However, this likely indicates an error in the initial probe tip diameter calibration. In order to verify this, these measurements were used to update the probe ball tip diameter calibration. This probing test was then repeated during a demonstration of the system. For this demonstration the system was dismantled, transported, and set up again in another location a number of days later. In this case, four measurements were taken and the measured diameters agree with the calibration within 17 µm.

Table 8: Measurements of the Mitutoyo CMM calibration ball taken during demonstration at Boeing Auburn

			Center Position (mm)		
Measurement	# Points	Diameter (mm)	X	Y	Z
1	10	19.972	242.493	71.46	272.751
2	10	19.99	242.488	71.496	272.761
3	10	19.995	242.512	71.383	272.723
4	10	19.982	242.528	71.514	272.785

Chapter 4: Conclusion

The flexible optical CMM design presented in this thesis is a promising device for on-machine inspection of parts. The system uses a high-speed target tracking camera design, based on that presented by Rao [10] with significant modifications to the data processing hardware and the communication interface. Implementing the EtherCAT communication interface between the cameras and the real-time computer allows the camera network to be easily reconfigured for different measurement applications. Camera positions can be changed and additional cameras can be added to cover occluded areas in the measurement volume or to increase measurement precision. The high measurement frequency of the system, which is designed for up to 8 kHz operation, allows large numbers of target measurements to be averaged to eliminate random noise. The software designed for the system performs the realtime position reconstruction with a program running in the TwinCAT operating system and streams this data to PolyWorks dimension checking software allowing

The calibration of the camera network was done using the procedure presented by Heikkila [9], and tested by Rao [10]. The results of the camera calibration indicate that the camera design is functioning correctly, providing similarly accurate measurements to those of Rao [10] using the same image sensor and lens combination.

A method was developed for the probe calibration. In this method, the probe is rotated about the tip center which is held still in a hole or cone. The probe tip location is then found by fitting spheres to the measured target trajectories. Simulation and measurement results show that this method was quite accurate, providing center location accuracy better than 10 µm.Following the identification of the probe tip location, a procrustes method is used to find an average of the measured target locations of the probe. This calibrated geometry is assumed to be more accurate than the measurement accuracy of the camera system, so that the camera system accuracy is relatively close to the measurement accuracy of the whole system.

The results for the whole system indicate good performance for the small measurement volume in which it was practical to test. The measured diameter of a small spherical artifact was repeatable to within 18 μm over a number of measurements. This is comparable to the specifications for the Creaform HandyProbe and AICON MoveInspect of 20 μm for a similar task.

Bibliography

[1] AICON 3D Systems GmbH, "MoveInspect HF | HR," [Online]. Available: http://www.aicon3d.com/fileadmin/user_upload/produkte/en/moveinspect/moveinspect_hf/pdf/Brochure_MoveInspect_HF_EN.pdf. [Accessed 20 June 2016].

[2] AICON 3D Systems GmbH, "MoveInspect Probing," [Online]. Available: http://www.aicon3d.com/fileadmin/user_upload/produkte/en/moveinspect/moveinspect_hr/pdf/MI_Probe_EN.pdf. [Accessed 20 June 2016].

[3] Creaform, "Portable Coordinate Measuring Machines: HandyProbe," 2016. [Online]. Available: http://www.creaform3d.com/en/metrology-solutions/coordinate-measuring-machines-handyprobe. [Accessed 21 June 2016].

[4] D. Gelbart and M. G. Laberge, "Optical coordinate measuring system for large objects". United States of America Patent US5305091 A, 19 April 1994.

[5] Faro, "Measuring Arm FaroArm - Features," [Online]. Available: http://www.faro.com/products/metrology/faroarm-measuring-arm/features#main. [Accessed 21 June 2016].

[6] W. T. Estler, K. L. Edmundson, G. N. Peggs and D. H. Parker, "Large-Scale Metrology - An Update," *CIRP Annals,* vol. 51, no. 2, pp. 587-609, 2002.

[7] T. Luhmann, "Close range photogrammetry for industrial applications," *ISPRS Journal of Photogrammetry and Remote Sensing,* vol. 65, no. 6, pp. 558-569, 2010.

[8] H. Broers and N. Jansing, "How precise is navigation for minimally invasive surgery?,"

International Orthopedics, vol. 31, no. 1, pp. 39-42, 2007.

[9] J. Heikkila and O. Silven, "A Four-step Camera Calibration Procedure with Implicit Image Correction," in *Proceedings of IEEE Computer Society Conference on Computer Vision and Pattern Recognition*, San Juan, 1997.

[10] N. Rao, "A Novel High-Speed Stereo-Vision System for Real-time Position Sensing," University of British Columbia, Vancouver, 2011.

[11] Y. Huang, "A High Accuracy CMOS Camera Based 3D Optical Tracking System Design," University of British Columbia, Vancouver, 2010.

[12] D. Rieke-Zapp, W. Tecklenburg, J. Peipe, H. Hastedt and C. Haig, "Evaluation of the geometric stability and the accuracy potential of digital cameras - Comparing mechanical stabilisation versus parameterisation," *ISPRS Journal of Photogrammetry and Remote Sensing,* vol. 64, no. 3, pp. 248-258, 2009.

[13] D. Umbach and K. N. Jones, "A Few Methods for Fitting Circles to Data," *IEEE Transactions on Instrumentation and Measurement,* vol. 52, no. 6, pp. 1881-1885, 2003.

[14] I. D. Coope, "Circle fitting by linear and nonlinear least squares," *Journal of optimization theory and applications,* vol. 76, no. 2, pp. 381-388, 1993.

[15] I. Kasa, "A Circle Fitting Procedure and Its Error Analysis," *IEEE Transactions on Instrumentation and Measurement,* vol. 61, no. 1, pp. 8-14, 1976.

[16] J. C. Gower and G. B. Dijksterhuis, Procrustes Problems, Oxford; New York: Oxford University Press, 2004.

[17] CMOSIS, "CMV12000 Product Sheet," [Online]. Available:

http://www.cmosis.com/products/product_detail/cmv12000. [Accessed March 2013].

[18] CMOSIS, "CMV20000 Product Sheet," [Online]. Available: http://www.cmosis.com/products/product_detail/cmv20000. [Accessed March 2013].

[19] CMOSIS, "CMV12000 Datasheet," CMOSIS, Antwerp, 2012.

[20] ON Semiconductor, "LUPA4000: 4 MegaPixel High Speed CMOS Image Sensor," ON Semiconductor, Phoenix, 2013.

[21] G. Cena, I. C. Bertolotti, S. Scanzio, A. Valenano and C. Zunino, "On the accuracy of the distributed clock mechanism in EtherCAT," in *2010 8th IEEE International Workshop on Factory Communication Systems (WFCS)*, Nancy, 2010.

[22] H. W. Johnson and M. Graham, High-Speed Digital Design: A Handbook of Black Magic, Upper Saddle River, New Jersy: Prentice Hall, 1993.

[23] Ed Fagan International, "Invar 36 Product Data," October 2013. [Online]. Available: http://www.edfagan.com/litPDF/Invar36_3-11-09F.pdf. [Accessed 29 May 2016].

[24] C. A. Swenson, "Recommended Values for the Thermal Expansivity of Silicon from 0K to 1000K," *Journal of Physical and Chemical Reference Data,* vol. 12, no. 2, p. 179, 1983.

[25] Performance Composites Ltd., "Mechanical Properties of Carbon Fibre Composite Materials," [Online]. Available: http://www.performance-composites.com/carbonfibre/mechanicalproperties_2.asp. [Accessed 10 Dec 2013].

[26] Dragon Plate, *Correspondence Regarding CTE,* 2013.

[27] AK Steel, "316/316L Stainless Steel Datasheet," 2007. [Online]. Available: http://www.aksteel.com/pdf/markets_products/stainless/austenitic/316_316L_Data_Sheet.p

df. [Accessed 5 December 2013].

[28] Goodfellow, "Ruby - online catalog source," 2013. [Online]. Available: http://www.goodfellowusa.com/A/Ruby.html. [Accessed 11 December 2013].

[29] F. C. S., A. Wods and D. Brizzi, "Hyper redundancy for accuracy enhancement in automated close range photogrammetry," *The Photogrammetric Record,* vol. 20, no. 111, pp. 205-217, 2005.

[30] A. Hedge, "Hand Tool Design - Cornell University Ergonomics Web," August 2013. [Online]. Available: http://ergo.human.cornell.edu/studentdownloads/DEA3250pdfs/Hand%20Tools.pdf. [Accessed 2 December 2013].

[31] Y. I. Abdel-Aziz and H. M. Karara, "Direct linear transformation into object space coordinates in close-range photogrammetry," in *Proceedings of Symposium on Close-Range Photogrammetry*, Urbana, IL, 1971.

Appendices

Appendix A Analysis of Thermal Expansion of the Probe Body

In order to estimate the thermal expansion of the metrology body, we assume that during measurement the probe will only be subject to temperature fluctuations of +/- 5C from the temperature at which it is calibrated.

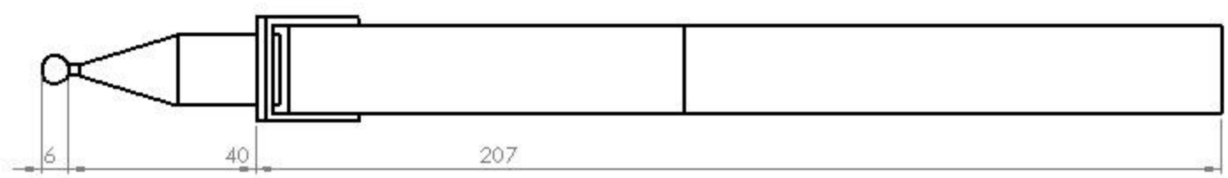

Figure 19: Metrology body profile and dimensions

Material	Length	CTE (microstrain/C)	Source
Carbon Fibre	207 mm	5 u/C *	[25] [26]
Stainless Steel	40 mm	17 u/C	[27]
Ruby	6 mm	6 u/C	[28]

*5 u/C is the worst case from [25]. Supplier indicates that 1u/C should be expected [26]

$$Expansion\ Constant\ of\ Structure$$

$$= .207m * 5 * \frac{10^{-6}}{C} + .04m * 17 * \frac{10^{-6}}{C} + 0.006m * 6 * \frac{10^{-6}}{C} = 1.75\frac{um}{C}$$

Worst case distortion during normal operation (+/- 5C) is therefore **8.75 µm**.

In the case where the user comes into direct contact with the metrology body, the user's body may be as much as 20C warmer than the probe. If we consider the structure warming up by this amount, the deformation would be ~35 µm. However, the user will be not warm the structure evenly, but will heat up only the area that they are touching. This uneven heating will lead the structure to bend while it expands, possibly causing a much greater error in measurement.

Appendix B Analysis of the Stiffness of the Probe Body

B.1 Horizontal Bending Case

To calculate the deflection of the metrology structure, we first consider the case where the metrology body is horizontal and lying in the orientation where it is least stiff.

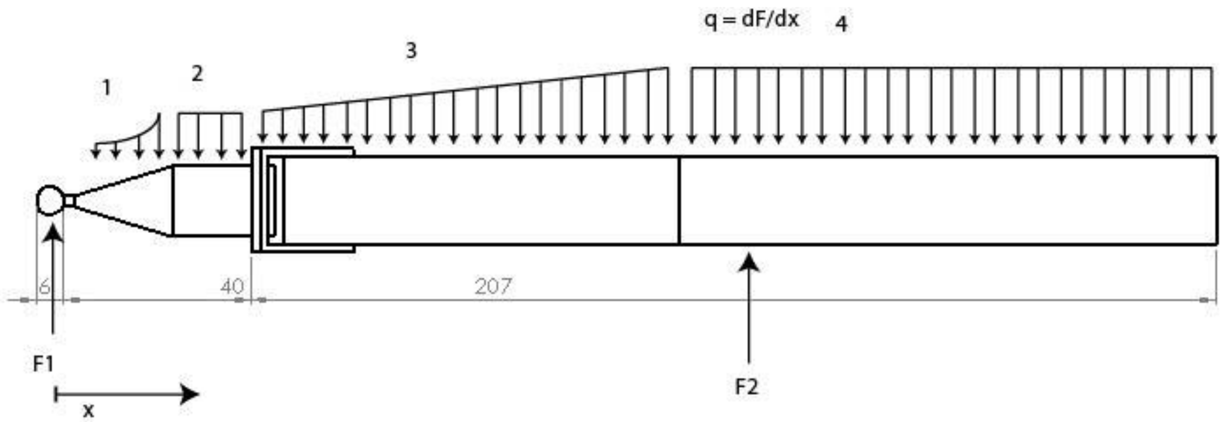

Figure 20: Loading of the metrology body

The figure above describes the loading of the probe. The distributed load is split into four regions. The expressions for the loads in each region are:

$$q_1 = \rho g \pi r^2 = \frac{8000kg}{m^3} * \frac{9.8N}{kg} * \pi * \left(1.25 * 10^{-3} + \frac{6.25}{21} * x\right)^2$$

$$q_2 = \rho g \pi r^2 = \frac{8000kg}{m^3} * \frac{9.8N}{kg} * \pi * (7.5 * 10^{-3}m)^2 = 13.85N/m$$

$$q_3 = \rho_{CF} gz * 3.3 * 10^{-3} + \rho_{Nom} gz * 19.05 * 10^{-3}$$

$$= \left(\frac{1500kg}{m^3} * 3.3 * 10^{-3}m + \frac{55kg}{m^3} * 19.05 * 10^{-3}m\right) * \frac{9.8N}{kg}$$

$$* (-8.88 * 10^{-3} + 1.22x)$$

$$q_4 = \rho_{CF} gz * 3.3 * 10^{-3} + \rho_{Nom} gz * 19.05 * 10^{-3}$$

$$= \left(\frac{1500kg}{m^3} * 3.3 * 10^{-3}m + \frac{55kg}{m^3} * 19.05 * 10^{-3}m\right) * \frac{9.8N}{kg} * 150 * 10^{-3}$$

$$= 8.817N/m$$

The area moment of inertia (I) is also different in each region. In regions 1 and 3, the area moment of inertia varies with x, while in regions 2 and 4 it is constant. The expressions for the two stylus regions are given below:

$$I_1 = \frac{\pi r^4}{4} = \frac{\pi}{4} * \left(1.25 * 10^{-3} + \frac{6.25}{21} * x\right)^4$$

$$I_2 = \frac{\pi r^4}{4} = \frac{\pi}{4} * (7.5 * 10^{-3})^4 = 2.5 * 10^{-9} m^4$$

In the honeycomb block, the carbon fiber panels are considered to take the entire bending load (Nomex core takes none), so the area moments of inertia are:

$$I_3 = 2 \int_{9.525*10^{-3}}^{11.175*10^{-3}} \int_0^z y^2 dz dy = \frac{2z}{3} * [(11.175 * 10^{-3})^3 - (9.525 * 10^{-3})^3]$$

$$= 354 * 10^{-9} * (-8.88E - 3 + 1.22x)$$

$$I_4 = 2 \int_{9.525*10^{-3}}^{11.175*10^{-3}} \int_0^{150*10^{-3}} y^2 dz dy = 53.14 * 10^{-9} m^4$$

Young’s Modulus of each region is also needed. For the stainless steel stylus regions it is assumed to be 200 GPa and for the CFRP honeycomb regions it is assumed to be 100 GPa [25]. In order to find the reaction forces, F1 at x=0 and F2 at x=145mm, we use a torque balance at each point. The moment balance at x=0 gives:

$$F2 * 0.145 = \int_0^{.245} q(x) x dx$$

Solving this by numerical integration in MATLAB (step size 0.001mm) gives F2 of 1.703 N.

The moment balance at x=145mm gives:

$$F1 * 0.145 = \int_{0}^{.245} q(x) * (0.145 - x)dx$$

Solving this gives F1 of 0.1985 N.

These two forces must then be used as boundary conditions for the expression of shear force (v) along the beam, in the region between F1 and F2:

$$v = \int_{0}^{x} qdx - F1$$

In the region beyond F2:

$$v = \int_{0}^{x} qdx - F1 - F2$$

The shear force profile is shown in the figure below.

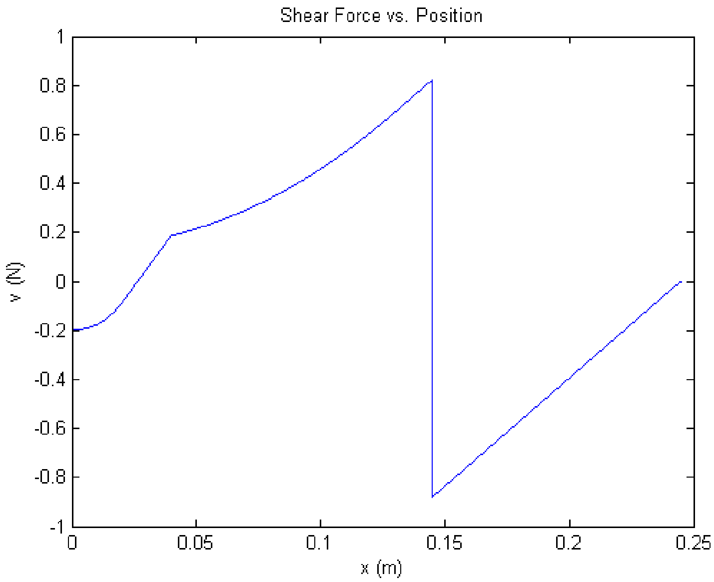

Figure 21: Shear force vs. position on metrology body

Since there are no external moments applied to the metrology body, the bending moment is just the integration of the shear force along the length:

$$M = \int_{0}^{x} v dx$$

The moment profile is:

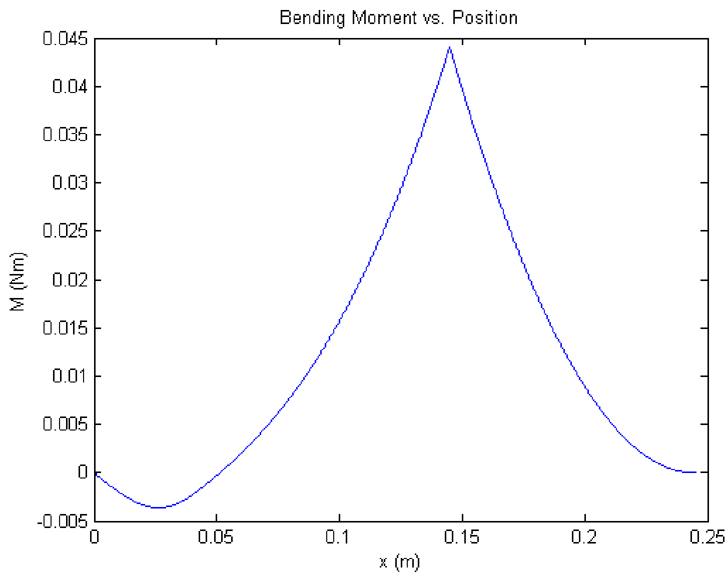

Figure 22: Bending moment vs. position on metrology body

The thin beam bending expression gives the relationship between bending moment and the curvature of the body:

$$\frac{d^2w}{dx^2} = \frac{-M}{EI}$$

So the slope (dw/dx) is:

$$\frac{dw}{dx} = \int_0^x \frac{-M(x)}{E(x)I(x)} dx + C$$

C is a constant that we pick so that the deflection is zero at the two constraint points (x=0, x=145mm).

The deflection (w) is:

$$w = \int_0^x \frac{dw}{dx} dx = \int_0^x \int_0^x \left(\frac{-M(x)}{E(x)I(x)} dx + C\right) dx$$

The deflection profile is:

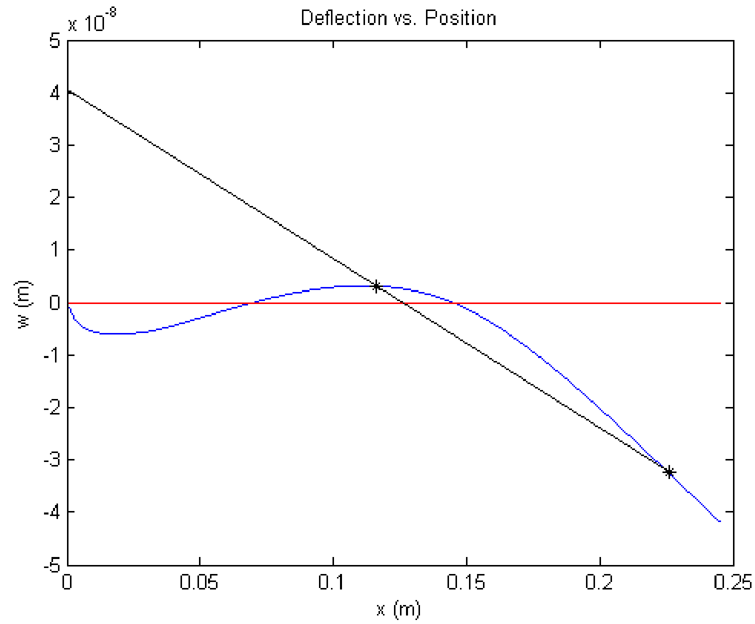

Figure 23: Deflection of metrology body and measurement error

Since we are concerned with the measurement error, we need to find the difference between the apparent and actual positions of the probe tip. To do this we trace a line through the positions of the LEDs. This line indicates the apparent orientation of the probe, its' Y-intercept indicates the apparent position of the probe tip relative to its' actual position at the origin. We see that the error is only **40 nm** which can be considered insignificant.

B.2 Vertical Case

In the previous case, the reaction force at the handle carries most of the weight. This minimizes the bending moment experienced in the weakest part of the metrology body, the stylus. It is therefore possible that the horizontal case is not the most conservative, so we should also check the case where the probe is standing upright, with the entire load supported by the stylus.

In this case, the deflections of the four individual sections can be considered separately.

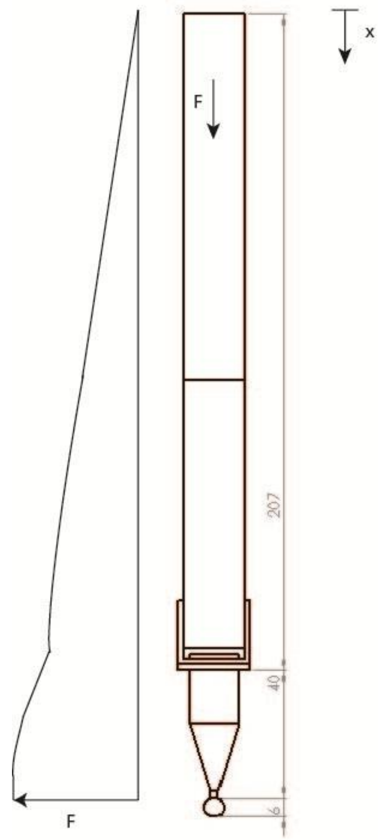

Figure 24: Vertical loading of the metrology body

The force at each point is plotted below:

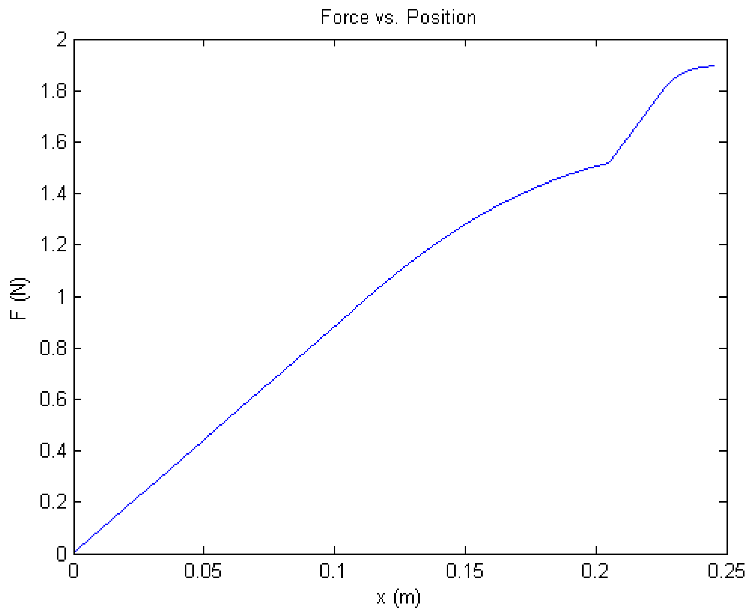

Figure 25: Force vs. Position in vertical position

The force varies as expected, reaching a maximum of ~1.9N at the bottom of the metrology body.

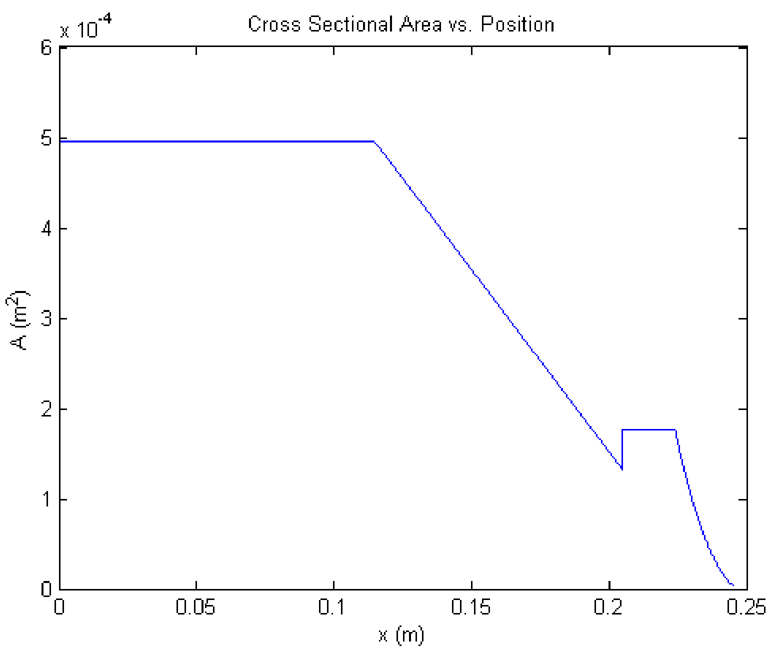

Figure 26: Cross Sectional Area vs. Position

Note that only the CFRP area is considered in the honeycomb block.

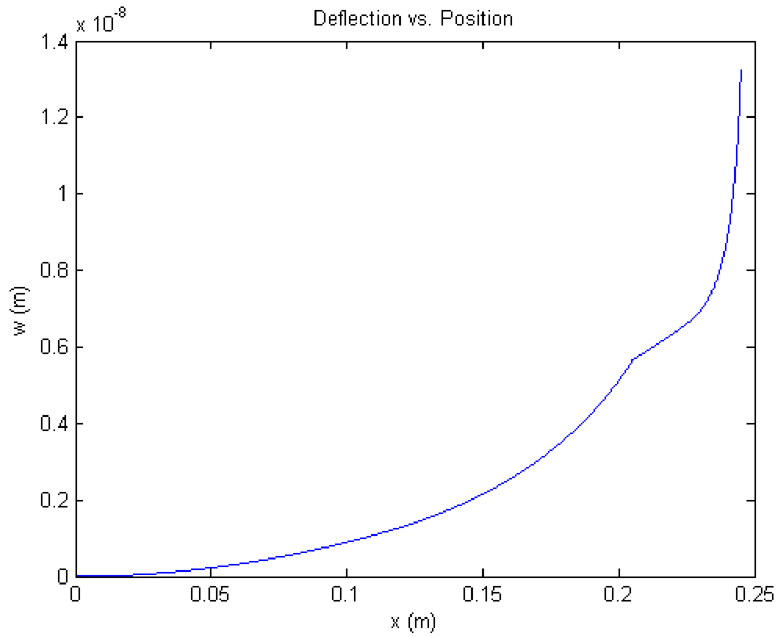

Figure 27: Deflection along the probe body

In this case as well as the horizontal case, the deflection is negligible.